Impacts of Updraft Size and Dimensionality on the Perturbation Pressure and Vertical Velocity in Cumulus Convection. Part II: Comparison of Theoretical and Numerical Solutions and Fully Dynamical Simulations

HUGH MORRISON

National Center for Atmospheric Research, Boulder, Colorado*

(Manuscript received 28 January 2015, in final form 17 July 2015)

ABSTRACT

This paper compares simple theoretical expressions relating vertical velocity, perturbation pressure, updraft size, and dimensionality for cumulus convection, derived in Part I, with numerical solutions of the anelastic buoyant perturbation pressure Poisson equation and vertical velocity w. A range of thermal buoyancy profiles representing shallow to deep moist convection are tested for both two-dimensional (2D) and three-dimensional (3D) updrafts. The theoretical expressions give similar results for w and perturbation pressure difference from updraft top to base Δp compared to the numerical solutions over a wide range of updraft radius R. The theoretical expressions are also consistent with 2D and 3D fully dynamical updraft simulations initiated by warm bubbles of varying width.

Implications for nonhydrostatic modeling in the ''gray zone,'' with a horizontal grid spacing Δx of O(1–10) km where convection is generally underresolved, are discussed. The theoretical and numerical solutions give a scaling of updraft velocity with R ($\sim\Delta x$) consistent with fully dynamical 2D and 3D simulations in the gray zone, with a rapid decrease of maximum w at relatively small R and a slower decrease at large R. These results suggest that an incorrect representation of perturbation pressure may be an important contributor to biases in convective strength at these resolutions. The theoretical solutions also provide a concise physical interpretation of the ''virtual mass'' coefficient in convection parameterizations and can be easily incorporated into these schemes to provide a consistent scaling of perturbation pressure effects with R, updraft height, and the buoyancy profile.

1. Introduction

Perturbation pressure exerts important effects on cumulus convection. It is well known that these effects depend in part on updraft width, and more specifically on the ratio of updraft width to height, with a downward-directed buoyant perturbation pressure gradient force in relatively wide updrafts compensating the upward thermal buoyant force to a greater degree than in narrower updrafts (e.g., Markowski and Richardson 2010). This has implications for the sensitivity of nonhydrostatic convection-permitting models to horizontal grid spacing Δx in the ''gray zone,'' with Δx of O(1–10) km, where convection is generally underresolved. Since convective overturning is forced to occur over larger scales as Δx is increased at these resolutions, this typically leads to fewer but wider updrafts compared to simulations with Δx of O(100) m (e.g., Bryan et al. 2003; Bryan and Morrison 2012; Morrison et al. 2015a). Quantitative understanding of the impact of these changes on the vertical velocity is critical, given its importance in driving microphysical processes and vertical fluxes of momentum, static energy, water, and chemical constituents. This is especially important since nonhydrostatic models at gray-zone resolutions are now widely employed for many applications, including operational numerical weather prediction (e.g., Kain et al. 2008; Lean et al. 2008; Weisman et al. 2008; Clark et al. 2012) and climate studies using global ''cloud resolving'' models (e.g., Miura et al. 2007) or embedding convection-permitting models in traditional large-scale general circulation models—that is, ''superparameterization'' (e.g.,

* The National Center for Atmospheric Research is sponsored by the National Science Foundation.

Corresponding author address: Hugh Morrison, National Center for Atmospheric Research, 3090 Center Green Drive, Boulder, CO 80301.
E-mail: morrison@ucar.edu

DOI: 10.1175/JAS-D-15-0041.1

Grabowski 2001; Khairoutdinov and Randall 2001; Tao et al. 2009).

Weisman et al. (1997, hereafter W97) performed two-dimensional (2D) and three-dimensional (3D) simulations of squall-line-type deep convection with fully coupled dynamics and moist physics and found strong sensitivity of the maximum vertical velocity w and horizontally averaged vertical fluxes of potential temperature and momentum to Δx between 1 and 20 km. There was a decrease in maximum w and slower storm evolution as Δx was increased but an increase in the domain-averaged vertical fluxes once the squall line reached a quasi-steady mature phase. They explained this sensitivity in part by a shift of the dynamics from being governed primarily by nonhydrostatic processes at Δx of $O(1)$ km to hydrostatic processes at Δx of $O(10)$ km. More recent studies have also shown that horizontal grid resolution can have a strong effect on simulated convective storm development and structure in the gray zone (e.g., Bélair and Mailhot 2001; Petch and Gray 2001; Petch et al. 2002; Adlerman and Droegemeier 2002; Bryan et al. 2003; Pauluis and Garner 2006; Gentry and Lackmann 2010; Fiori et al. 2010; Bryan and Morrison 2012; Verrelle et al. 2015; Morrison et al. 2015a). For example, Bryan and Morrison (2012) found a roughly 20% decrease in total upward mass flux with an increase in mean updraft size and decrease in number between Δx of 1 and 4 km, while Petch et al. (2002) showed a delay in convective development as Δx was increased.

Another aspect of perturbation pressure is its effect on the sensitivity of updraft strength to dimensionality (2D vs 3D). Several studies have shown that 2D updrafts tend to be weaker than their 3D counterparts (e.g., Wilhelmson 1974; Schlesinger 1984; Lipps and Hemler 1986; Tao et al. 1987; Redelsperger et al. 2000; Phillips and Donner 2006; Zeng et al. 2008). For example, Phillips and Donner (2006) reported that cloudy updrafts were 20%–50% stronger in 3D than 2D, with substantial impacts on vertical profiles of cloud liquid and ice and hence surface and top-of-atmosphere radiative fluxes. Understanding physical mechanisms for these differences and how they relate to perturbation pressure is important given the continued wide use of 2D models.

Another important aspect of perturbation pressure is its treatment in cumulus convection schemes. For parameterizing w using simplified plume models embedded in these schemes, perturbation pressure effects are typically either neglected or included in a simple way by scaling the buoyancy with a constant "virtual mass" coefficient. The simplicity of this method is attractive but it is lacking in physical justification. Settings for the virtual mass coefficient are often ad hoc or tuned, with the buoyancy typically reduced by a factor of ~1–3 (e.g., Simpson and Wiggert 1969; Gregory 2001; Bechtold et al. 2001; Bretherton et al. 2004; Jakob and Siebesma 2003; Neggers et al. 2009; see Table 1 in Wang and Zhang 2014). A few studies have fit the virtual mass coefficient to large-eddy simulations applied to shallow cumulus convection (de Roode et al. 2012; Wang and Zhang 2014), but the generality of this approach is unclear. Park (2014) included a virtual mass coefficient that has an exponential dependence on updraft radius R, from 1 at $R = 0$ to ⅓ at $R = \infty$. However, both the single normal mode and general theoretical solutions in Morrison (2016, hereafter Part I) suggest that perturbation pressure effects on w have a scaling of the form $(1 + R^2/H^2)^{-1/2}$, where H is the updraft height. On the other hand, nearly all schemes incorporate effects of R and/or H on entrainment, often assuming an entrainment parameter that scales as $1/R$ or $1/z$, where z is height (e.g., Simpson and Wiggert 1969; Kain and Fritsch 1990; Donner 1993; de Rooy and Siebesma 2010). Moreover, some schemes allow R to vary or use an ensemble of plumes with different R to generate a spectrum of plume characteristics through modification of entrainment (e.g., Kain 2004; Kuang and Bretherton 2006). While particular values of R should perhaps not be taken too literally in these schemes since they are primarily used to generate variability in the entrainment rate (cf. Kain 2004), neglecting the scaling of perturbation pressure with R and H but including a dependency of entrainment on R or z can lead to a physical inconsistency. Given these issues, refining the treatment of perturbation pressure effects can improve the physical basis and self-consistency of convection parameterizations.

Part I of this study presents simple analytic expressions relating perturbation pressure and updraft velocity to R, H, and convective available potential energy (CAPE) for 2D and axisymmetric quasi-3D updrafts. In the current paper, Part II, these theoretical solutions are compared with direct numerical calculations of the anelastic buoyant perturbation pressure Poisson equation. The theoretical solutions are also compared to 2D and 3D fully dynamical updraft simulations initiated with warm bubbles of varying sizes. Implications for nonhydrostatic modeling in the gray zone are discussed, including sensitivity to Δx and dimensionality. Application of the theoretical expressions for improving perturbation pressure effects in cumulus parameterizations is also described.

The remainder of the paper is organized as follows. Section 2 describes the methodology for numerically solving the buoyant perturbation pressure Poisson equation. Results including comparison of the analytic expressions with the numerical solutions and with fully dynamical updraft simulations are presented in section 3. Discussion

of relevance to gray-zone modeling and convection parameterizations is given in section 4, and a summary and conclusions are presented in section 5.

2. Methodology for numerical solution

To demonstrate the impact of updraft size and dimensionality on perturbation pressure and w and test the theoretical approach derived in Part I, the perturbation pressure field corresponding to a prescribed distribution of thermal buoyancy B is solved numerically. Updrafts are treated as isolated, steady-state regions of $B > 0$ in an environment with $B = 0$, consistent with the simplified conceptual model of buoyant updrafts used for the theoretical derivation in Part I. The dynamic perturbation pressure p_D is neglected in the numerical calculations [p_D is defined by $\nabla^2 p_D = -\nabla \cdot (\rho \mathbf{u} \cdot \nabla \mathbf{u})$ in the anelastic system, where $\mathbf{u}$ is the wind vector and ρ is a background-state air density, which is horizontally homogeneous but varies with height]. Thus, the perturbation pressure field is calculated by numerically solving the anelastic buoyant perturbation pressure Poisson equation [see (6) in Part I]:

$$\nabla^2 p = \nabla^2 p_D + \nabla^2 p_B \approx \frac{\partial(\rho B)}{\partial z}, \tag{1}$$

where p_B is the buoyant perturbation pressure. Neglecting p_D is reasonable since fully dynamical simulations indicate that $\partial p_D/\partial z$ has a limited impact on the average acceleration[1] of w compared to $\partial p_B/\partial z$ in the updraft core in weakly sheared environments that are the focus of this study (see discussion in Part I). Vertical acceleration at the updraft center is calculated from the derived p_B field and specified B as explained below. Hereafter the subscript B is dropped and p will refer to p_B unless otherwise stated.

This approach is inspired by Parker (2010), who calculated the p field and acceleration numerically from a specified distribution of B to discern the impacts of updraft tilting on buoyant perturbation pressure and w. Numerical solutions herein are calculated for both 3D and 2D. For 3D, updrafts are represented by a steady-state cylinder of positively buoyant air (relative to the environment). For 2D, updrafts are represented by an analogous slab of positively buoyant air. Other features associated with convective updrafts that affect buoyancy, such as cold pools and gravity waves, are neglected for simplicity. Updrafts are assumed to be upright. The idea is to mimic the fundamental features of convective updrafts in an environment with weak vertical wind shear.

Equation (1) is solved to obtain p on a domain with 129 grid points along each of the horizontal and vertical dimensions for either 2D or 3D. The domain is periodic in the horizontal direction(s). Solutions are calculated using a spatial discretization of 100 or 200 m vertically (depending upon the updraft height) and 1/10 of the updraft radius horizontally (finer discretization does not noticeably affect results). A multigrid iterative solver with Gauss–Seidel point relaxation and a tolerance threshold of 10^{-6} for the maximum relative error is employed.

Upper and lower boundary conditions are determined as follows. At the surface and top of the atmosphere, if $B = 0$, then $\partial p/\partial z = 0$ since $w = 0$ there (for inviscid flow). Thus, it is reasonable to specify $\partial p/\partial z = 0$ at the upper and lower boundaries. However, when combined with the periodic lateral boundary conditions this Neumann problem leads to nonuniqueness. (This can be easily seen in the case of a horizontally homogeneous distribution of B, in which case the Poisson equation reduces to the one-dimensional hydrostatic perturbation pressure equation and the conditions $\partial p/\partial z = 0$ at the top and bottom give a nonunique profile of p.) This leads to difficulty in convergence and large drift in the values of p using the iterative Poisson solver. However, an additional physical constraint is that $p = 0$ at the top of the atmosphere. If we choose a domain top sufficiently high and use the mixed boundary conditions of $p = 0$ at the top and $\partial p/\partial z = 0$ at the bottom, as applied in the 1D model of Holton (1973), this allows for faster convergence of the solver. Moreover, at the hydrostatic limit, when the buoyancy perturbation is applied horizontally across the entire domain, there is a closer balance of $\partial p/\partial z$ and ρB using the condition $p = 0$ compared to using $\partial p/\partial z = 0$ at the domain top. It is important to point out that using Neumann versus mixed boundary conditions has little impact on gradients of p that are relevant to the dynamics (less than few percent except near the hydrostatic limit) and is, therefore, not particularly important for this study.

The p field is derived for various spatial structures and magnitudes of B (see section 3a). Since the buoyancy and hence perturbation pressure is assumed to be symmetric around the updraft center, the implied wind field at the updraft center has $u = v = 0$, where u and v are the horizontal components of air velocity. Thus, profiles of w at the updraft center can be calculated by simple vertical integration without complications from horizontal motion. This is done using the steady-state vertical momentum equation given by (11) in Part I together with the calculated profile of $\partial p/\partial z$ and specified buoyancy at the updraft center. Integration over z

[1] "Acceleration" here and elsewhere in the paper refers to parcel acceleration in a Lagrangian framework; i.e., D/Dt.

TABLE 1. Summary of the thermodynamic soundings. "Maximum w" indicates the maximum thermodynamic vertical velocity equal to $\sqrt{2\text{CAPE}}$, and H is the difference in height between the level of neutral buoyancy and the level of free convection.

Name	CAPE (J kg^{-1})	Maximum w (m s^{-1})	H (km)	Reference
DC3	1051.4	45.9	11.2	M. Barth (2014, personal communication)
WK	2715.6	73.7	10.6	Weisman and Klemp (1982)
J2007OK	7364.2	121.4	13.8	Morrison et al. (2015b)
M2008OK	4828.7	98.3	12.2	Dawson et al. (2014)
RICO	341.2	26.1	5.8	vanZanten et al. (2011)
BOMEX	35.5	8.4	1.2	Siebesma et al. (2003)

is done using a simple forward Euler scheme with a lower boundary condition of $w = 0$ at the level of free convection (LFC; defined as the lowest level with $B > 0$) and a vertical grid discretization of 100 or 200 m.

3. Results

a. Sounding data

To analyze the theoretical and numerical solutions for w and the perturbation pressure difference between the level of neutral buoyancy (LNB) and LFC Δp a number of thermodynamic soundings over a wide range of conditions are used to generate various buoyancy profiles representing shallow to deep moist convection. The buoyancy is calculated based on adiabatic ascent of the most unstable parcel, relative to an environment with $B = 0$ and neglecting entrainment and condensate loading. Although these buoyancy profiles are calculated based on ascent from the LFC to the LNB, this is not required since the numerical calculations and theoretical expressions can be applied to any buoyancy profile (section 3e compares the theoretical expressions with fully dynamical simulations of growing updrafts before they reach the LNB). A summary of the six soundings is given in Table 1, and skew-T diagrams for each sounding are shown in Fig. 1. Some soundings are from individual sonde measurements, while others are composites of multiple sondes or analytic idealizations. These particular soundings were chosen because most of them have been widely analyzed and used for model initial conditions in previous studies. Note that some soundings were significantly sheared (e.g., M2008OK, an environment supporting supercell storms) and, therefore, inconsistent with the underlying assumption of an unsheared environment, but are tested here to include a wide range of thermodynamic conditions.

b. Numerical solution of Poisson p_B equation

Examples of the numerical solution for p in 3D are shown in Figs. 2 and 3 for the WK and RICO soundings, respectively. For these calculations, the horizontal buoyancy distribution within the updraft is assumed to follow $B(r) = \cos[\pi r/(2R)]$, where r is the horizontal distance from the updraft center and is referred to as "COS." Two other distributions are also tested: $B(r) = \cos^2[\pi r/(2R)]$ ("COS2") and a top-hat distribution ("TOP"). All soundings illustrate a structure of $p > 0$ above the level of maximum buoyancy (LMB) and $p < 0$ below this level, consistent with the discussion of the perturbation pressure equation in Part I (section 3a). Maxima and minima are located near the LNB and LFC, respectively. The magnitude of p and hence its vertical gradients increase with R, all else equal. There is also a clear increase of the magnitude of p with CAPE, as expected. The maximum p (associated with the nonhydrostatic pressure) increases with R/H up to $R/H \sim 3$. For R/H larger than ~3, the maximum p decreases and approaches 0 as the hydrostatic limit is reached, when the field of total p is equal to that of the hydrostatic perturbation pressure. On the other hand, the minimum p at the LFC, associated with the hydrostatic perturbation pressure, decreases monotonically as R/H is increased. The perturbation pressure field for the WK sounding in 2D is shown in Fig. 4. All else being equal, the magnitude of the perturbation pressure is larger in 2D than 3D. Overall, the perturbation pressure fields for the COS2 and TOP buoyancy distributions are similar to COS, except for a reduction in the perturbation pressure magnitude for COS2 and an increase for TOP (not shown).

The u and w acceleration vectors calculated directly from the p and B fields (i.e., equal to $-\rho^{-1}\partial p/\partial x$ for u acceleration and $-\rho^{-1}\partial p/\partial z + B$ for w) are also shown in Figs. 2–4. Large acceleration occurs within the updraft, as expected, with downward acceleration occurring just beyond the updraft lateral edge. Downward acceleration is at a maximum near the updraft edge and decreases in magnitude away from the updraft. There is also a region of upward acceleration above the LNB associated with an upward-directed p gradient force, since the maximum p is located at the LNB and decreases with height above. However, it should be kept in mind that in this simple framework we have assumed $B = 0$ in the environment. In a more detailed framework, feedback between B and vertical motion in a statically stable environment would lead to generation

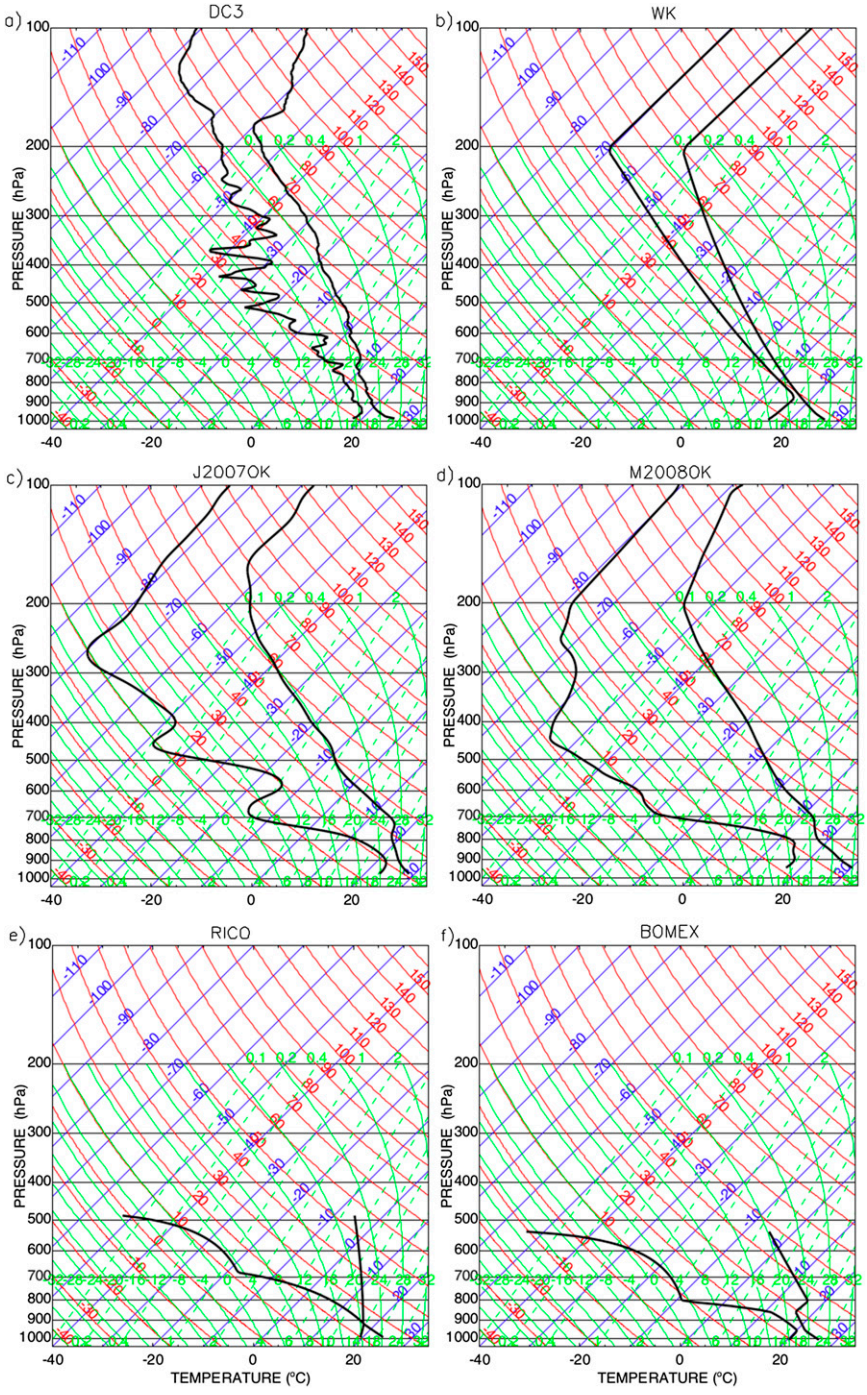

FIG. 1. Skew-T diagrams for the six thermodynamic soundings listed in Table 1.

and propagation of gravity waves; thus, caution should be exercised when interpreting the acceleration field outside of the updraft. Also note that in this framework, the u and w acceleration fields associated with B and p_B are not strictly consistent with mass continuity over the domain. This can be easily understood by noting that the total ($p_D + p_B$) perturbation pressure must be consistent with mass continuity (since it is derived by taking the divergence of the momentum equation), implying that if p_D is nonzero then the acceleration field calculated solely from p_B (and B) will be inconsistent with mass continuity. This is not expected to be important in the updraft core since $|\partial p_D/\partial z|$ is generally small relative to $|\partial p_B/\partial z|$ there (see discussion in Part I, section 2)

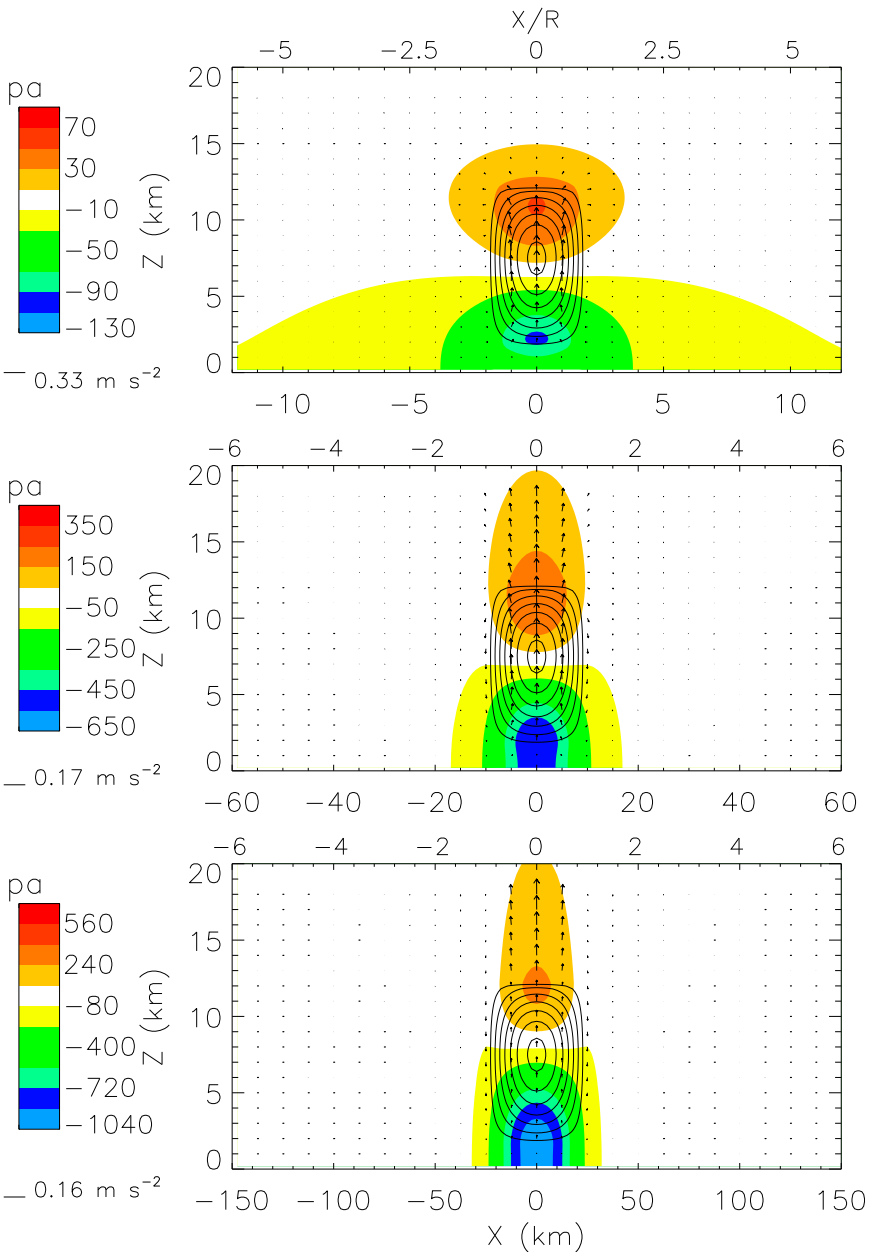

FIG. 2. Vertical cross section of the perturbation pressure (color contours) calculated from the Poisson solver, thermal buoyancy (black contour lines; interval of 0.05 m s^{-2}), and acceleration vectors for the WK sounding, COS horizontal buoyancy distribution, updraft radius of (top) 2, (middle) 10, and (bottom) 25 km, and 3D. The cross section is taken at the location of maximum buoyancy in the y direction. Note that only part of the domain is shown.

but is likely more important for downward acceleration along the updraft edge.

c. *Comparison of the theoretical and numerical solutions*

The theoretical solutions for w at the LMB w_M, w at the LNB w_N, and Δp following (20), (27), and (28) for 3D and (31)–(33) for 2D in Part I are compared to numerical calculations of the p_B field and w at the updraft center for the three horizontal buoyancy distributions discussed above. The parameter α in the theoretical expressions, equal to the ratio of w horizontally averaged across the updraft to that at the updraft center (see Part I, section 3), cannot be calculated directly from the numerical solutions. However,

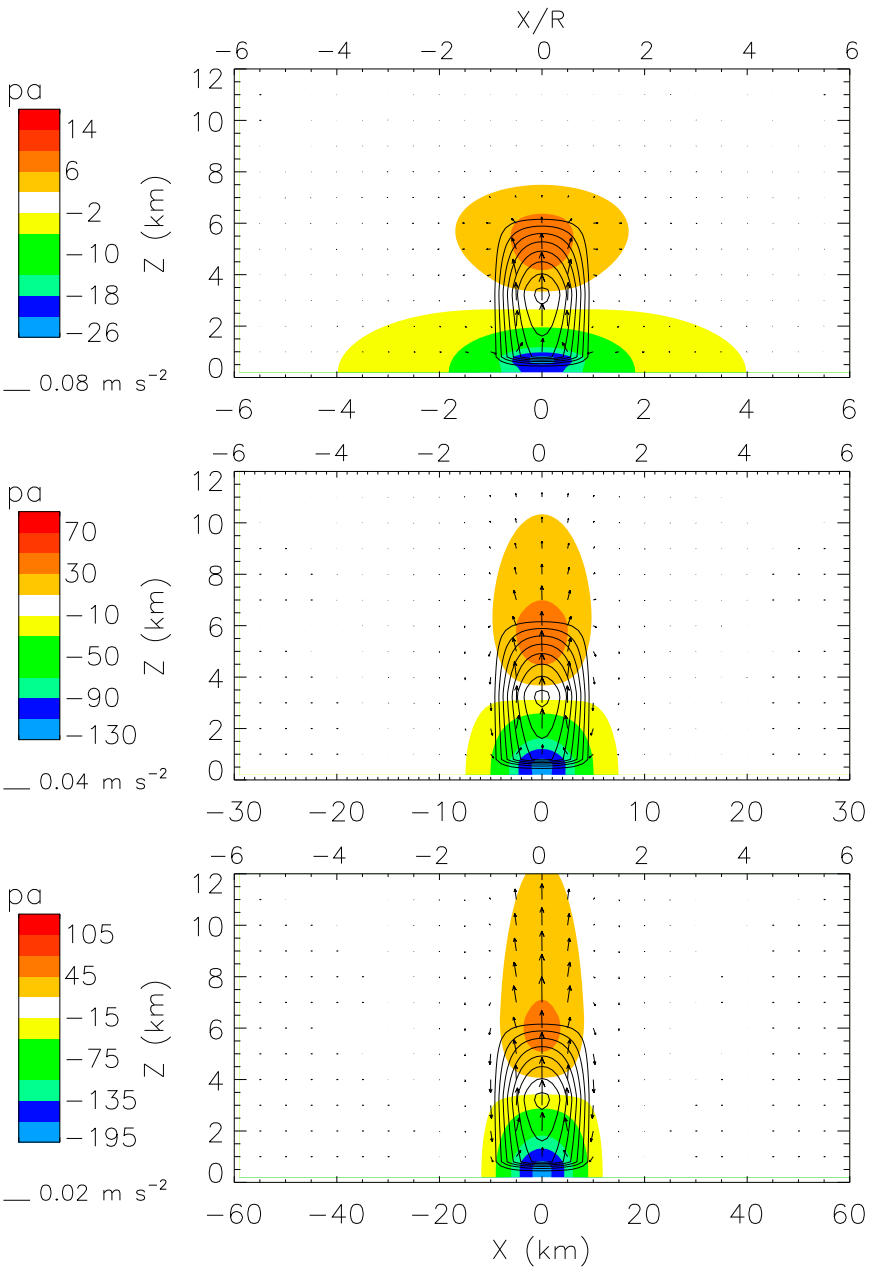

FIG. 3. As in Fig. 2, but for the RICO sounding and updraft radius of (top) 1, (middle) 5, and (bottom) 10 km. Contour interval for thermal buoyancy (black contour lines) is 0.01 m s^{-2}.

α is calculated directly from the 2D and 3D fully dynamical updraft simulations described in section 3e. These simulations have similar horizontally averaged B in 2D and 3D but give somewhat larger α for 3D than 2D (~0.8 vs 0.5). On the other hand, the tests here have horizontally averaged B about 25%–40% smaller in 3D than 2D for COS and COS2. Thus, for simplicity the same α is applied for 2D and 3D here, estimated by taking the ratio of B averaged along a horizontal line from the updraft center to its edge to B at the updraft center. This gives α of 1, 0.6367, and 0.5 for TOP, COS, and COS2, respectively.

Figures 5–8 show the 2D and 3D w_M and w_N as a function of R for each sounding for the COS and TOP buoyancy distributions. COS2 produces similar results as COS but with w larger by about 10%–15% and is, therefore, not shown. Figure 9 presents a comparison of the theoretical and numerical Δp for COS (TOP and COS2 give similar results; not shown).

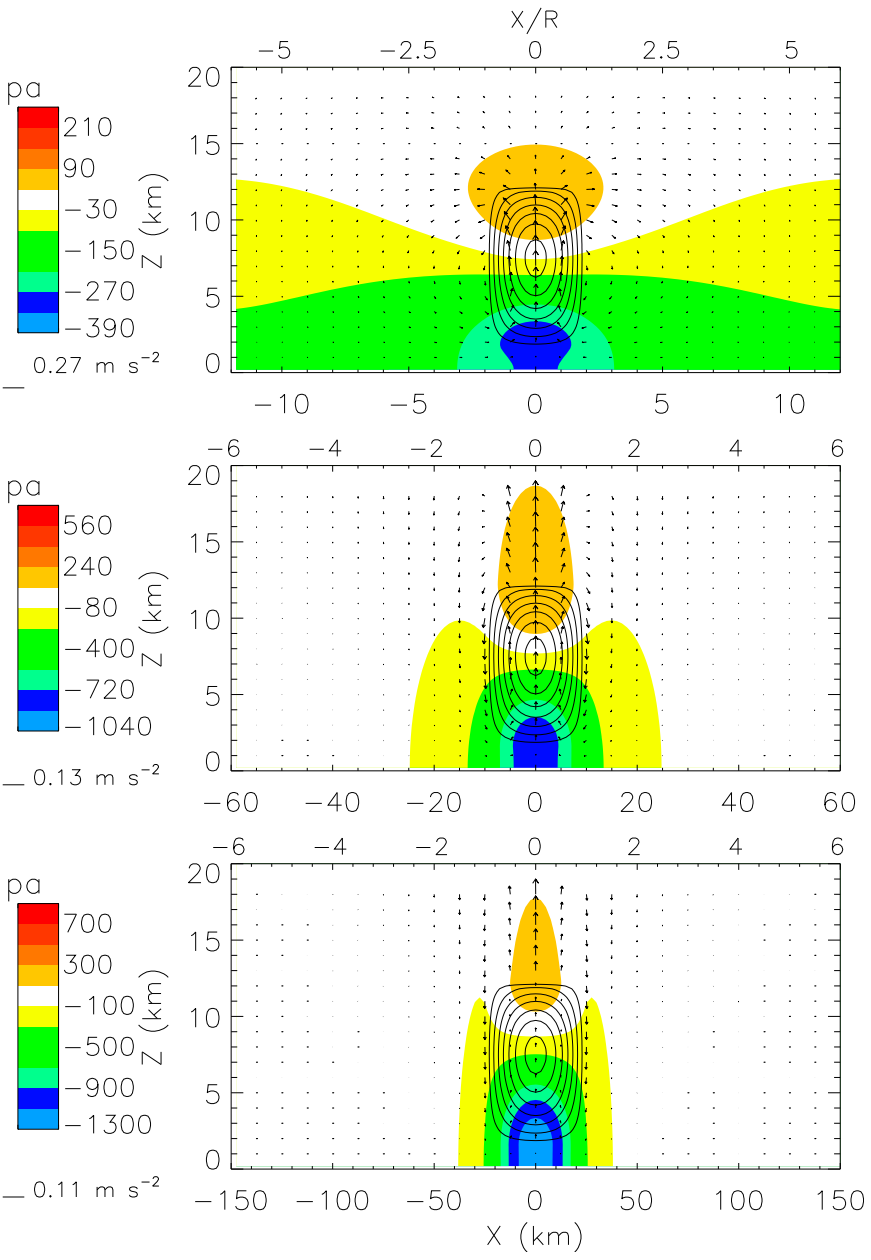

FIG. 4. As in Fig. 2, but for 2D instead of 3D.

Overall, the theoretical and numerical calculations are in close agreement. Notably, the theoretical solutions capture the increase of Δp and decrease of w for 2D compared to 3D. For $R/H \sim 1$ in 3D, the analytic and numerical solutions show a decrease of w from the theoretical thermodynamic maximum of about 25%–40% for 3D and 40%–60% for 2D. For R/H less than ~0.2, perturbation pressure effects are small, with a reduction of w relative to the thermodynamic maximum (equal to $\sqrt{2\text{CAPE}}$) of less than ~10% even in 2D. The value of Δp increases sharply with R for R/H less than about 1.5–2 but asymptotically approaches the hydrostatic value of Δp (approximately equal to $\overline{\rho}$CAPE, where $\overline{\rho}$ is the vertically averaged air density) for larger R/H.

Most differences between the theoretical and numerical Δp, especially for the deeper cases, are from using the Boussinesq approximation in the theoretical derivation (see Part I). Additional tests applying the Boussinesq instead of anelastic approximation to the numerical calculations show a closer correspondence with the theoretical Δp (Fig. 10). However, using the Boussinesq

versus anelastic approximation has only a limited impact on w. Even for the deepest case (J2007OK), there is negligible impact on w at the LNB (less than a few percent difference), less than ~15% difference at the LMB, and ~30% difference near the LFC. Moreover, there is almost no dependence of w on the magnitude of ρ for the Boussinesq numerical solutions. These results are consistent with the theoretical derivation; there is a cancellation of ρ in the pressure term $\Delta p/\rho$ in the vertical momentum equation since ρ also appears in the numerator of the theoretical expression for Δp [see (28) in Part I], implying a limited dependence of w on ρ.

d. Vertical profiles of w

This subsection compares vertical profiles of w from the theoretical and numerical solutions. For 3D, theoretical profiles of w from the LFC to LMB are calculated using the value of CAPE at a given height with the pressure scaling at the LMB given by (20) in Part I. From the LMB to the LNB, w is given by a scaling of CAPE at a given height that is linearly weighted between the scaling at the LMB and that at the LNB, given by (27) in Part I, as an approximate way to reflect smoothness of the pressure field. Thus, for 3D updrafts

$$w(z) = \sqrt{2\left(1+\frac{\alpha^2R^2}{H_1^2}\right)^{-1}\int_{z_{\rm LFC}}^{z} B\,dz} \quad z \le z_{LMB} \quad \text{and} \tag{2}$$

$$w(z) = \sqrt{2\left[\left(1+\frac{\alpha^2R^2}{H_1^2}\right)+\frac{(z-z_{\rm LMB})}{H_2}\left(\frac{2\alpha^2R^2}{H^2}-\frac{\alpha^2R^2}{H_1^2}\right)\right]^{-1}\int_{z_{\rm LFC}}^{z} B\,dz} \quad z > z_{LMB}, \tag{3}$$

where H_1 is the difference in height between the LMB and LFC and H_2 is the difference in height between the LNB and LMB. Analogous expressions are derived for 2D.

Figure 11 presents results for the COS buoyancy distribution and three different values of R/H (⅓, 1, and 2). Overall, the theoretical w profiles show a close correspondence to the numerical calculations and well represent differences between 2D and 3D. Interestingly, the profile of w is "flattened" as R/H increases and pressure effects become important, meaning that $\partial w/\partial z$ becomes nearly constant with height even though there is a sharp decrease of B above the LMB. This result is seen in both the numerical and theoretical solutions. For the numerical solutions this occurs partly because of the fundamental vertical asymmetry of the B distribution; the region with $B > 0$ is located nearer the surface than the top, driving asymmetries in the vertical distribution of $\partial p/\partial z$ (it also occurs partly because of the vertical variation of ρ). Thus, this asymmetry is evident even in tests (not shown) with a symmetric B profile (meaning the profile from the LMB to LNB is a mirror image of that from the LFC to LMB), constant ρ, and the condition $\partial p/\partial z = 0$ at both the upper and lower boundaries. For the theoretical results this asymmetry arises from the different scalings for w_M and w_N. This generally leads to a relatively larger pressure reduction of w below the LMB than above, as a result of the approximation $w_M/H_1 \sim w_N/H$ for calculating Δp in the theoretical derivation (see Part I, section 3). This approximation well captures vertical asymmetries in the numerical solutions.

e. Comparison with fully dynamical updraft simulations

A direct comparison of the theoretical solutions with fully dynamical simulations of individual updrafts using the nonhydrostatic, compressible CM1 (Bryan and Fritsch 2002) is challenging because of difficulties in controlling updraft width in the simulations, especially for wide updrafts, and the role of entrainment, which was not explicitly included in the theoretical derivation. Moreover, the simulations are time evolving with growing updrafts, while the theoretical solutions assume steady-state analogous to the plume conceptual model. However, the perturbation pressure in CM1 is nearly diagnostic from the buoyancy and wind fields at any instance in time (it is not exactly diagnostic because CM1 is compressible, but the impacts of compressibility are expected to be negligible given the small Mach number of the flow; cf. Emanuel 1994). Thus, the perturbation pressure from the model and theoretical solutions can be compared with minimal complications from time dependency. On the other hand, $\partial w/\partial t$ appears directly in the vertical momentum equation and this term can be of the same magnitude as the other terms, meaning there is a time dependence for w that is neglected in the steady-state theoretical solutions. Nonetheless, for maximum w in the updraft center

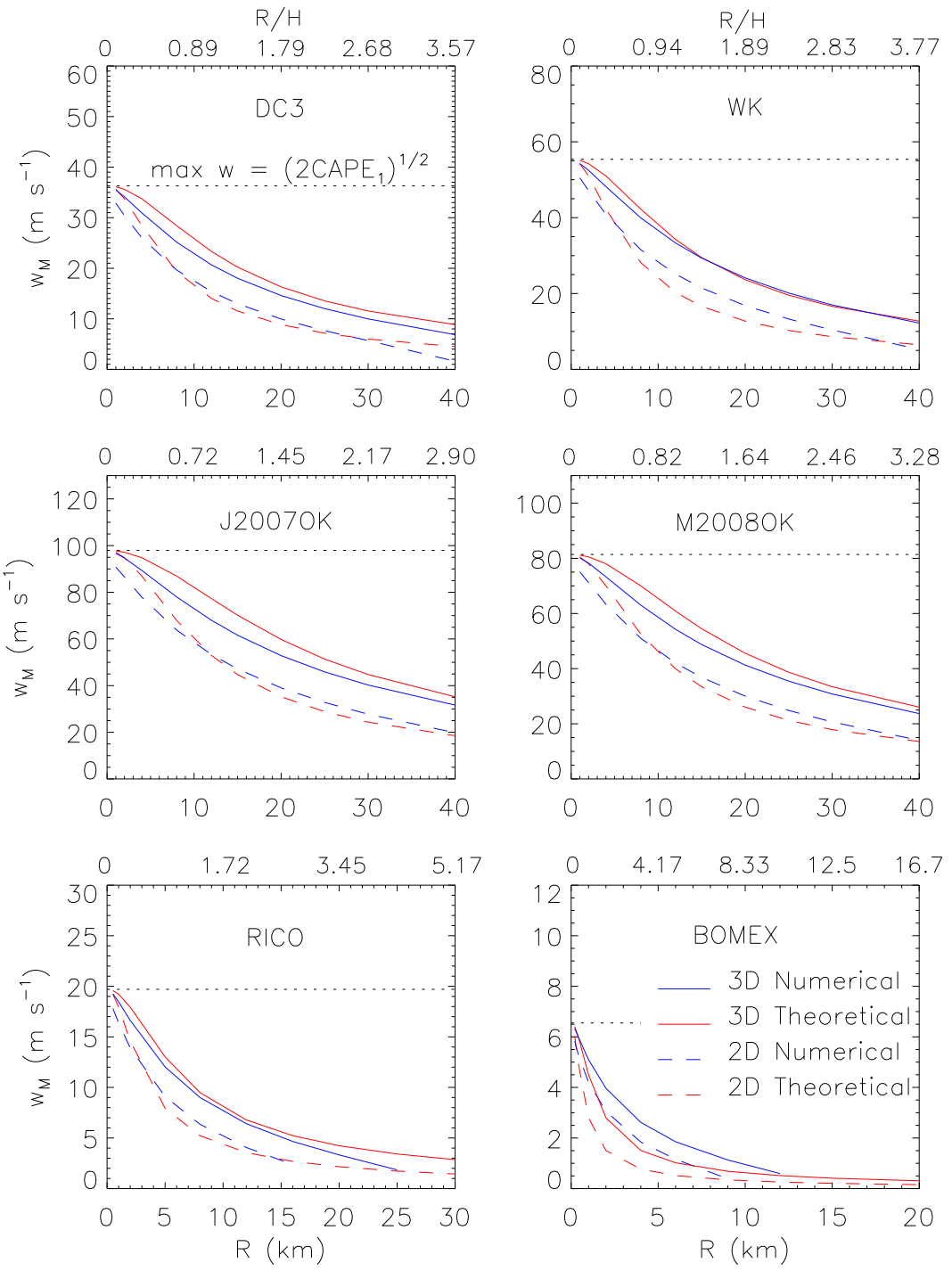

FIG. 5. Theoretical (red) and numerical (blue) calculations of w_M as a function of R for the six thermodynamic soundings and COS buoyancy distribution. Solid and dashed lines indicate calculations for 3D and 2D, respectively. The thermodynamic maximum w at the LMB given by $\sqrt{2\text{CAPE}_1}$ is shown by the horizontal dotted line.

the theoretical solutions are reasonably similar to the simulations as shown below. By analyzing the simulations shortly after release of the bubbles (within the first ~10–17 min), complications from entrainment are minimized given that it takes finite time for entrainment to have a large effect on the wind and buoyancy fields.

The model setup follows that in Part I, with 200-m horizontal and vertical grid spacings over a domain

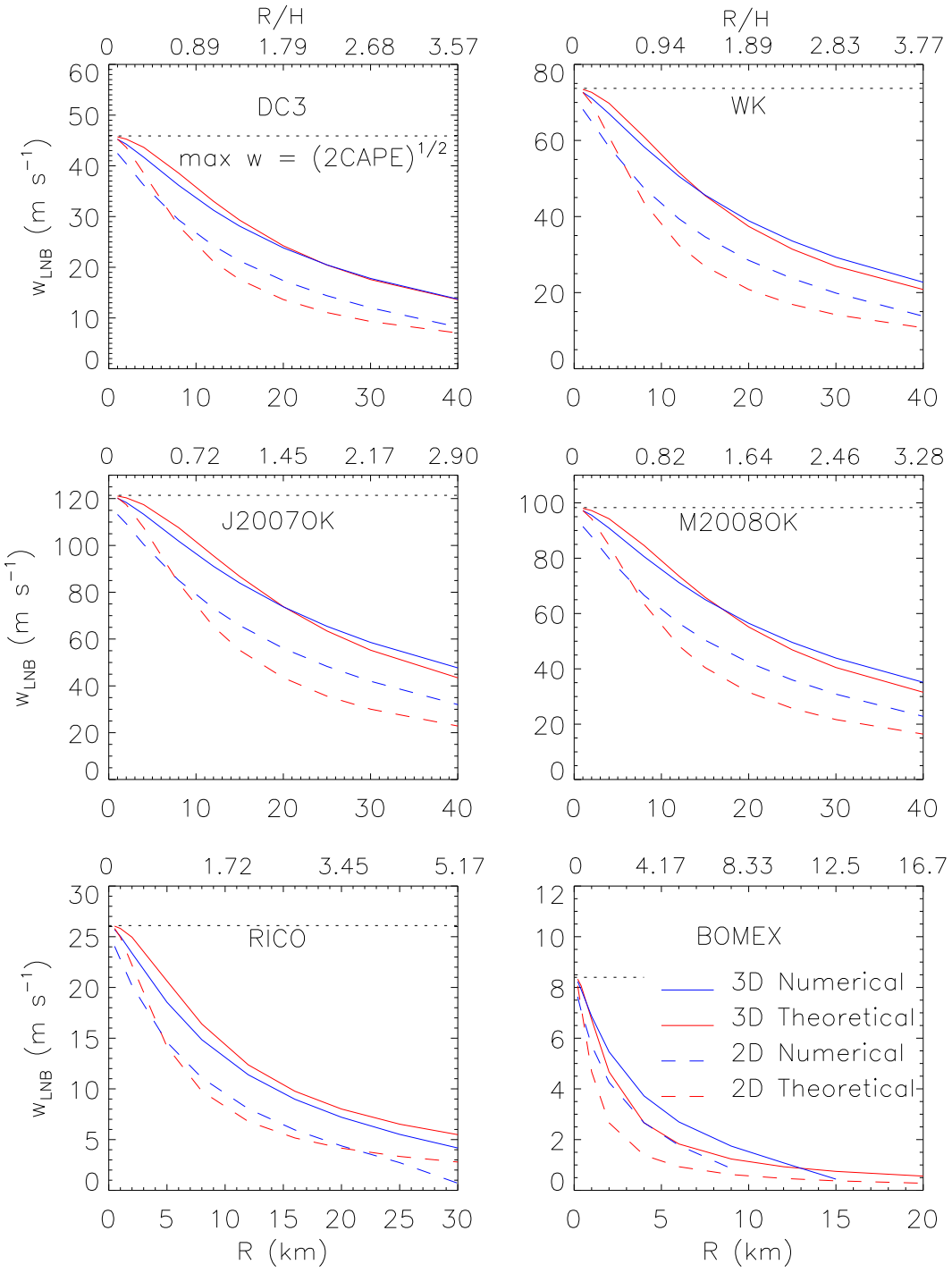

FIG. 6. As in Fig. 5, but for w_N.

$60 \times 60 \times 20\,\text{km}^3$ in 3D and $60 \times 20\,\text{km}^2$ in 2D. Convection is initiated by applying warm bubbles that have a maximum perturbation potential temperature of 2 K (relative to the background state), vertical radius of 1.5 km, centered at an altitude of 1.5 km, and with perturbation potential temperature decreasing as a cosine function from the thermal center to its edge. Initial environmental thermodynamic conditions follow from the analytic sounding of Weisman and Klemp (1982), and the domain is initially motionless.

Three simulations each for 2D and 3D are performed with different horizontal radii for the initial warm bubbles: 1.5, 3, and 10 km. Since updraft growth is slower for

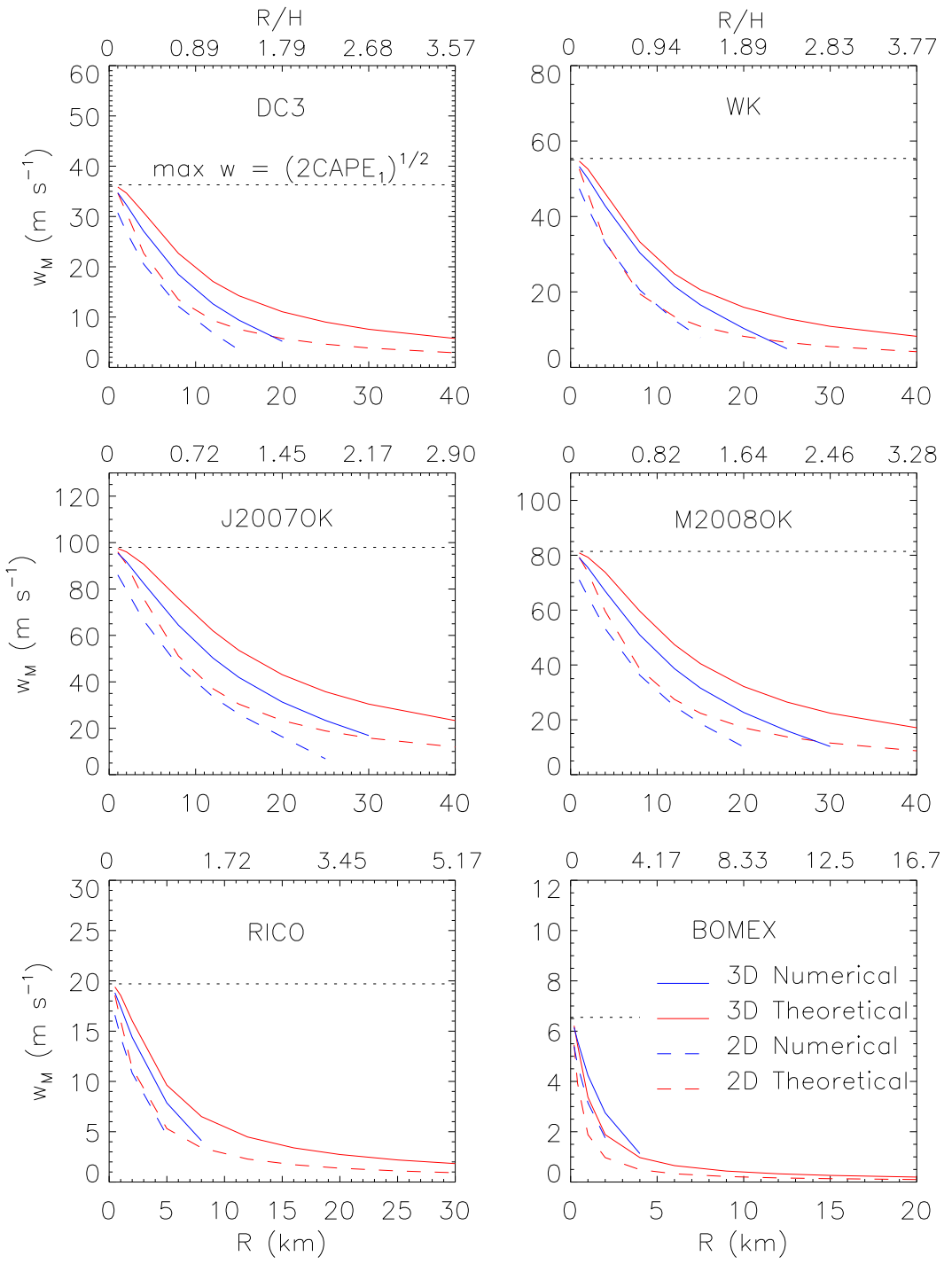

FIG. 7. As in Fig. 5, but for the TOP horizontal buoyancy distribution.

relatively wide updrafts, narrow updrafts are analyzed at earlier times than wider updrafts: 400 (550), 460 (600), and 760 (1020) s for the 1.5-, 3-, and 10-km initial bubble radii simulations for 3D (2D). These particular times were chosen because they give similar updraft top heights and buoyancy profiles in the updraft center among the simulations. Note, however, that overall results including comparison of the simulated and theoretical perturbation pressure and w do not depend much on the particular time analyzed within the first ~10–20 min of the simulations. Vertical cross sections of the total perturbation pressure and w across the

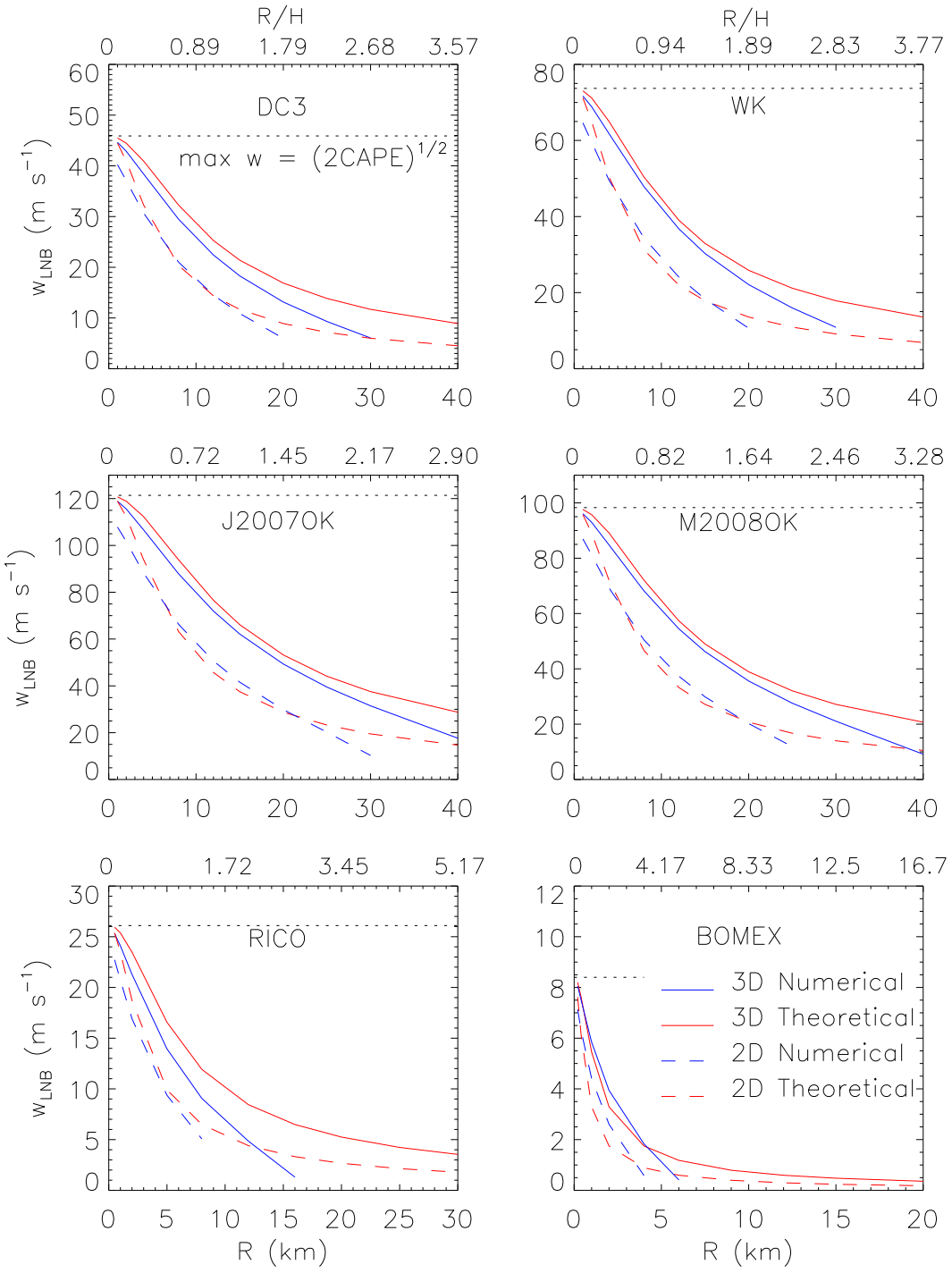

FIG. 8. As in Fig. 5, but for w_N and the TOP horizontal buoyancy distribution.

updraft center for the 3D simulations at these times are illustrated in Fig. 12.

Parameters used in the theoretical expressions for w and Δp [see (20), (27), and (28) for 3D and (31)–(33) for 2D in Part I] are taken directly from the simulations, including CAPE, R, H, ρ, and α. For consistency, CAPE is calculated by vertically integrating the buoyancy profile at the updraft center, including the effects of condensate loading, which reduce CAPE by approximately ⅓ in all of the simulations, as opposed to that based on adiabatic parcel ascent from the LFC to LNB. The values of R and H are calculated by the region with

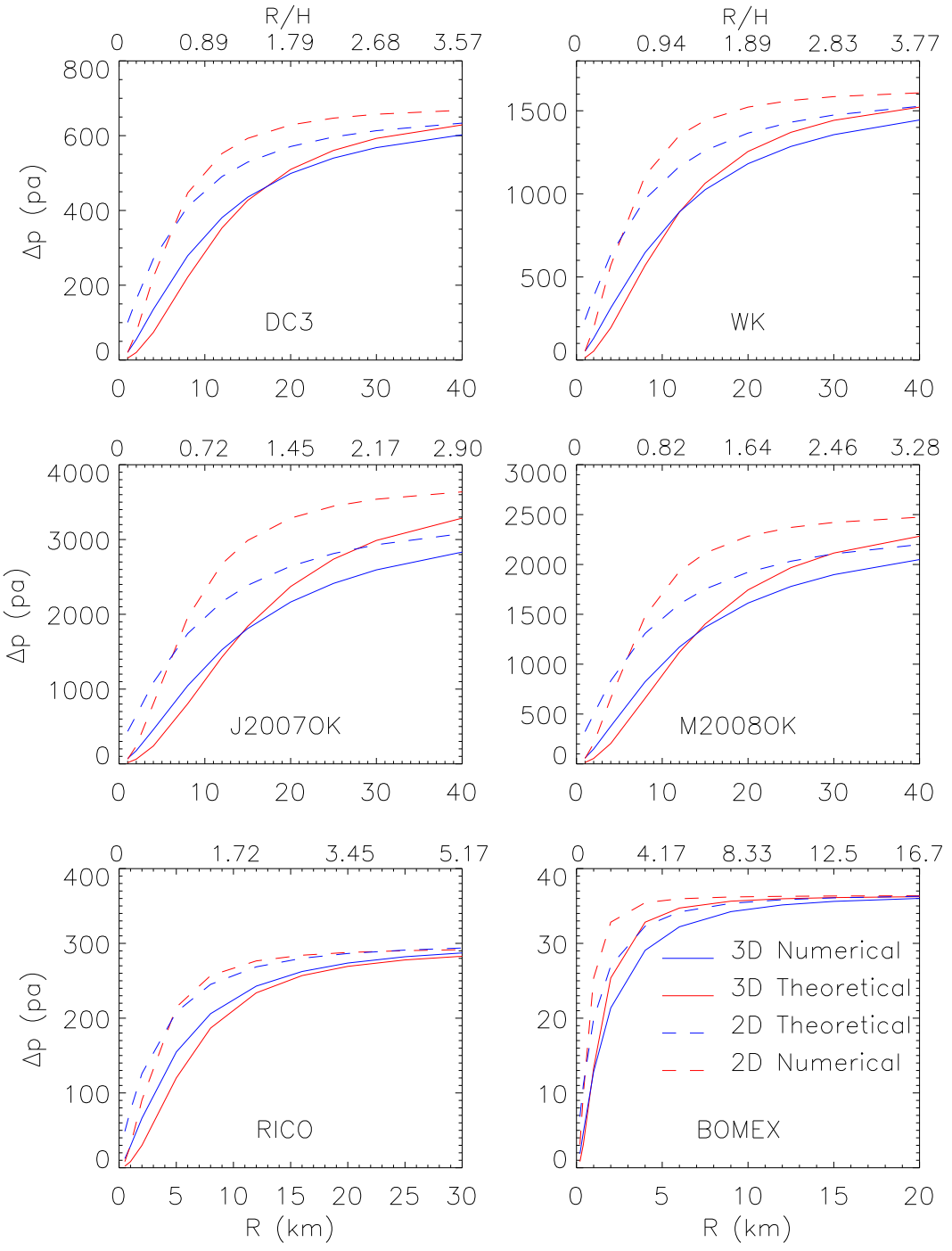

FIG. 9. Theoretical (red) and numerical (blue) calculations of the perturbation pressure difference between the LNB and LFC as a function of updraft radius for the six thermodynamic soundings and COS buoyancy distribution. Solid and dashed lines indicate calculations for 3D and 2D, respectively.

perturbation potential temperature greater than 1 K, which corresponds well to the region of positive buoyancy between the updraft base and top (defined by the vertical levels for which B goes to ~0). Since updraft width is not constant with height, an average R is calculated and used in the theoretical expressions. The value of α is calculated directly from the ratio of w averaged horizontally across the updraft to the value at the updraft center at each vertical level and then averaged over height. There is a small overall decrease of α with

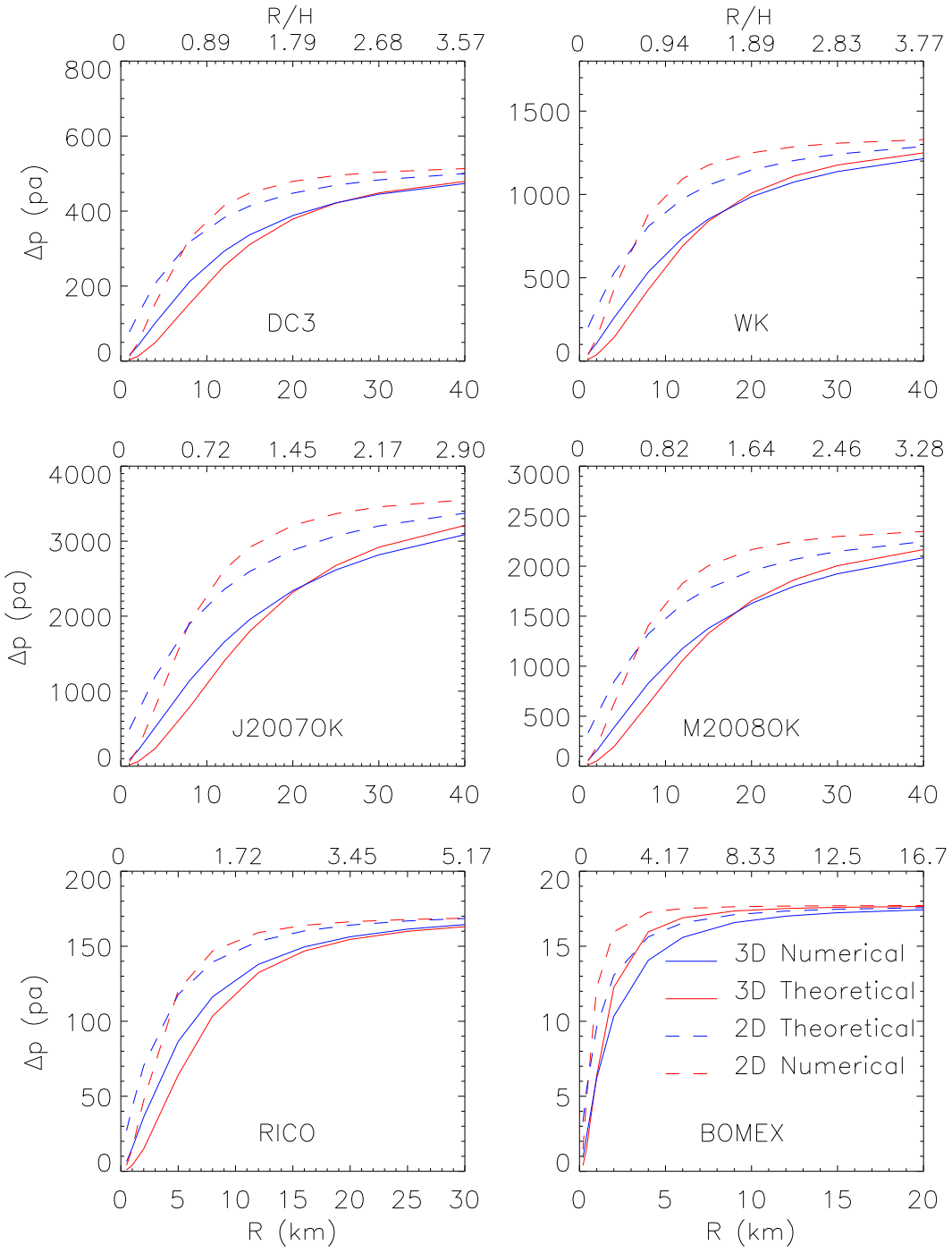

FIG. 10. As in Fig. 9, but using the Boussinesq approximation (constant $\rho = 0.5\,\mathrm{kg\,m^{-3}}$) for both the numerical and theoretical calculations.

height from about 0.95 to 0.7 in the 3D simulations below the LMB and an increase above. In contrast, α tends to increase more uniformly with height for 2D. Overall, α is larger for 3D than 2D (~0.8 vs 0.5), even though the ratio of horizontally averaged B to that at the updraft center is similar. The maximum w from the analytic theoretical expressions is taken as the larger of either w_N or w_M (here w_N and w_M refer to the vertical velocity at the updraft top and the LBM), since w_M can be larger than w_N despite the smaller integrated buoyancy up to this level because of the vertical asymmetry of the pressure scaling of w.

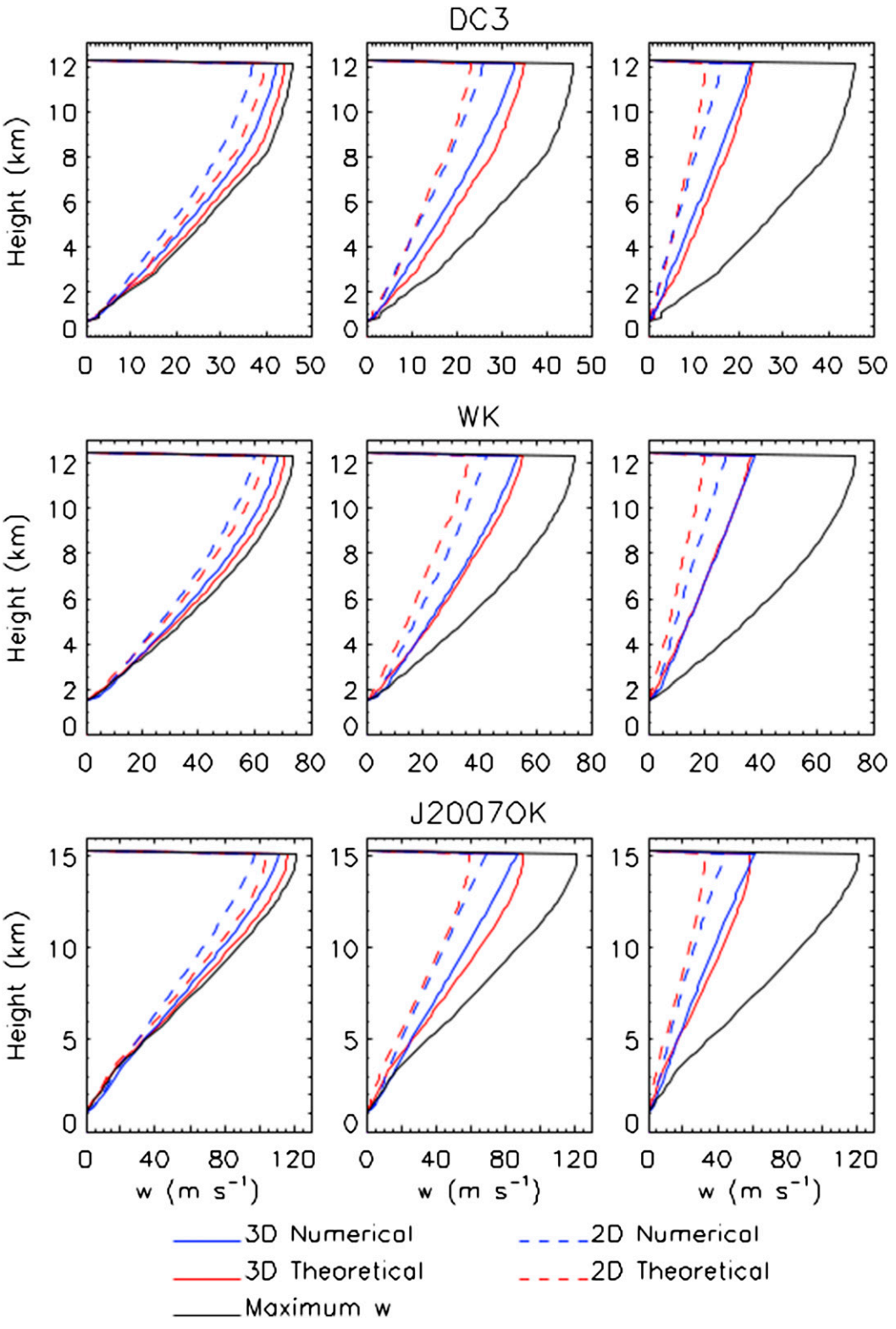

FIG. 11. Vertical profiles of theoretical (red) and numerical (blue) vertical velocity for normalized updraft radius, R/H, of (left) $\frac{1}{3}$, (center) 1, and (right) 2 for the six soundings and COS horizontal buoyancy distribution. Solid and dashed lines indicate calculations for 3D and 2D, respectively. The profile of thermodynamic maximum w given by $\sqrt{2\text{CAPE}}$ is shown by the black line. Height is above ground level.

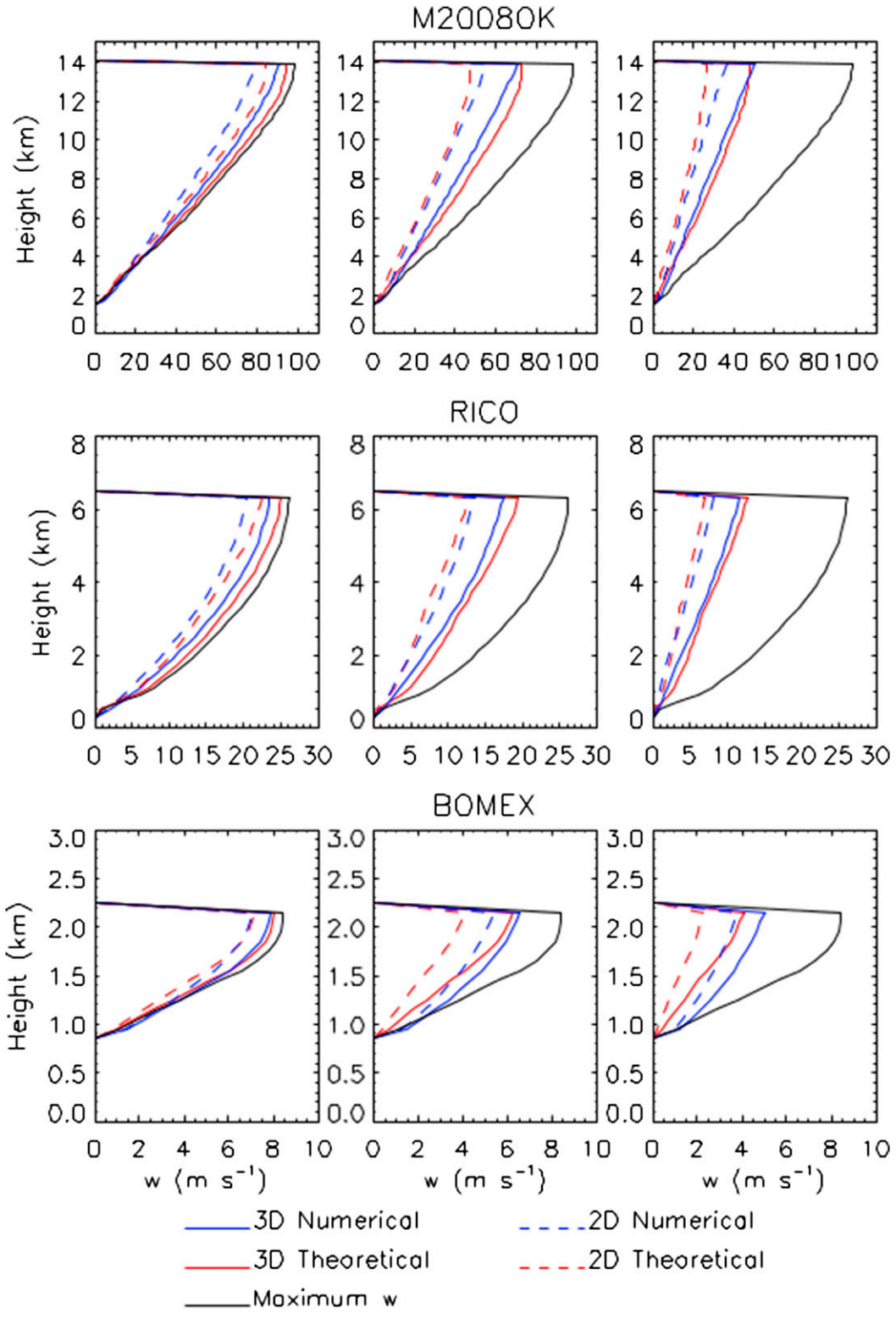

FIG. 11. (*Continued*)

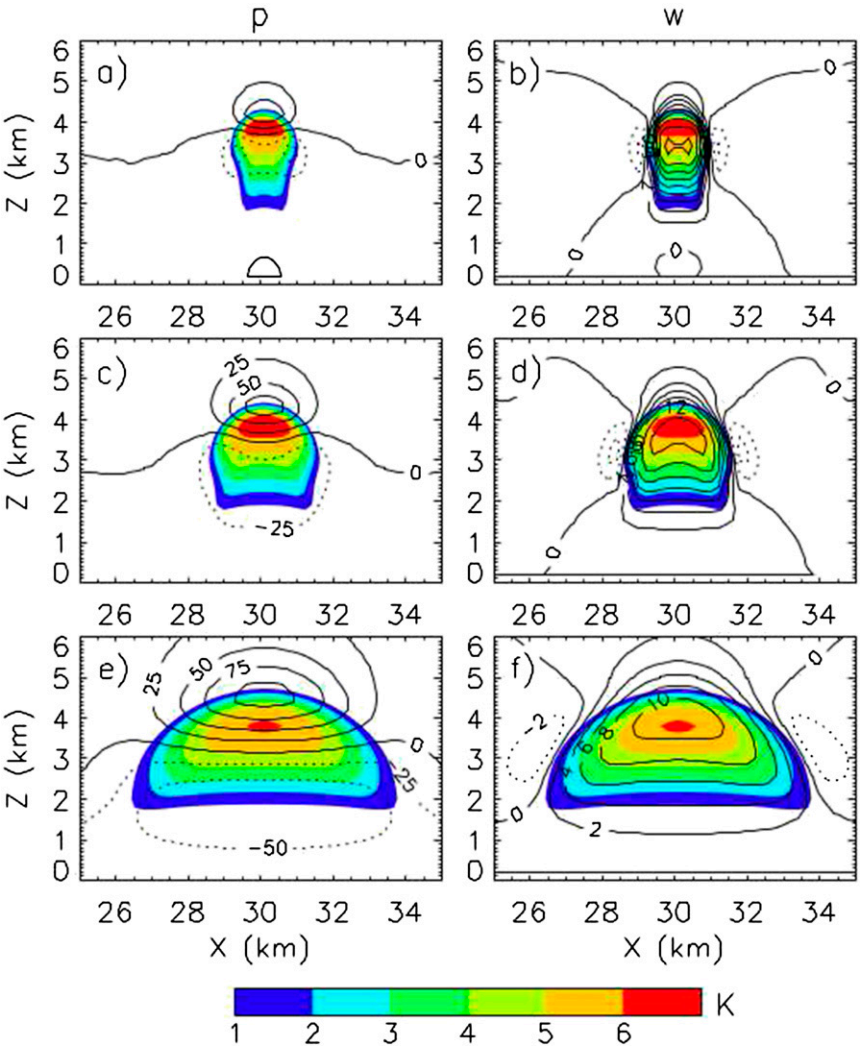

FIG. 12. Vertical cross section at the updraft center from fully dynamical 3D simulations of an isolated convective updraft initiated with a warm bubble of radius (a),(b) 1.5, (c),(d) 3, and (e),(f) 10 km, similar to Fig. 3.1 in Markowski and Richardson (2010). (left) Total perturbation pressure p and (right) vertical velocity w. Color contours show the perturbation potential temperature (relative to the initial environment) in all panels. The contour interval is 25 hPa for p and 2 m s^{-1} for w. Results are shown for times when the cloud top reaches ~4.5 km in height: 400, 460, and 760 s for the initial bubble radii of 1.5, 3, and 10 km, respectively. Note that only part of the domain is shown.

Results are summarized in Table 2 for 3D and Table 3 for 2D. The mean values of R from the three simulations are 1.5 (2.2), 2.5 (3.3), and 5.7 (5.4) km, corresponding to R/H of 0.6 (0.9), 1.0 (1.3), and 2.0 (2.1), respectively, for 3D (2D). The theoretical solutions show a close correspondence to values from the simulations, within ~15% for Δp and ~25% for maximum w for all of the 2D and 3D cases. The theoretical solutions are able to capture differences between 2D and 3D. However, the location of maximum w in the simulations is somewhat lower than in the conceptual model underpinning the theoretical derivation, occurring just below the LMB for the narrowest updraft and just above the LMB for the widest one. This likely reflects, in part, the role of local vertical gradients of p_D in the updraft center discussed in Part I (section 2) that were neglected in the theoretical derivation. The simulated w values are also fairly small near the updraft top likely because of momentum entrainment (especially from numerical mixing), as well as the fact that the simulations are time evolving and it takes a finite amount of time to accelerate w as the updraft top grows.

The region of positive buoyancy (relative to the environment) becomes highly deformed once entrainment begins playing a dominant role in the simulations after

TABLE 2. Summary of results from the 3D fully dynamical simulations and theoretical solutions with three different warm-bubble radii to initiate convection. Results are illustrated at 400, 460, and 760 s for the 1.5-, 3-, and 10-km initial bubble radii simulations, respectively, when the updraft top reaches ~4.5 km in height. Mean updraft radius R, height H, CAPE, and α are calculated from the simulations. The perturbation pressure difference from the updraft top to its bottom (defined as the heights at which buoyancy goes to zero) Δp and maximum updraft velocity w at the updraft center are shown from the simulations (SIM) and the theoretical solutions (TH).

					Δp (hPa)		Max w (m s^{-1})	
Initial warm-bubble radius (km)	R (km)	H (km)	CAPE (J kg^{-1})	α	SIM	TH	SIM	TH
1.5	1.5	2.4	241	0.78	76	66	18.1	18.8
3	2.5	2.6	261	0.82	123	125	14.4	15.7
10	5.7	2.8	290	0.77	179	207	11.0	9.8

~10–20 min (Fig. 13), especially for 2D. This leads to a complicated structure of the buoyancy field with regions of strongly positive buoyancy wrapped around the region of low dynamic pressure along the lateral updraft edge, making it difficult to clearly define an updraft R. Nonetheless, if a consistent definition of R is applied to all of the simulations at these later times (taken as the length from the updraft center to the outermost edge of the region of large perturbation potential temperature, defined by the 6-K isotherm), overall the theoretical expressions are consistent with the simulations. This is illustrated by comparing the simulated and theoretical Δp and w when the updraft top reaches 9–10 km in height (Tables 4 and 5). The theoretical expressions give larger Δp and smaller w for 2D compared to 3D seen in the simulations and capture the decrease in Δp from the widest to the narrowest initial bubbles. However, quantitative differences between the theoretical expressions and the simulations are larger than earlier in the simulations, especially for Δp. This is presumably because of the complicated structure of the buoyancy field after entrainment begins to dominate.

4. Discussion

a. *Implications for model sensitivity to horizontal grid resolution*

As discussed in the introduction, convective overturning is forced to occur over larger scales as the model grid resolution is increased in the gray zone, with Δx of O(1–10) km where moist atmospheric convection is generally underresolved. This typically leads to updrafts that are too wide and few in number. This is clearly seen, for example, in the simulations of Bryan and Morrison (2012, see their Fig. 2), which show a mean updraft width that approximately scales with Δx. Based on the results presented herein, as Δx and hence R increase there is an increased downward-directed perturbation pressure gradient force and weaker updrafts, all else being equal. These results suggest, therefore, that an incorrect representation of perturbation pressure from spuriously wide updrafts may be an important contributor to biases in convective strength in gray-zone models. At relatively coarse resolutions, with Δx of O(10) km, the theoretical and numerical calculations suggest biases in w of a factor of 2 or more, assuming a real updraft width of O(1) km.

These points are illustrated by comparing the maximum w from fully dynamical, nonhydrostatic 2D and 3D simulations of W97 (see their Figs. 16 and 17) and the numerical and theoretical w_N over a range of R (Fig. 14). This approach is similar to Pauluis and Garner (2006), who compared theoretical scalings for w as a function of updraft size with fully dynamical simulations using varying Δx. W97 employed the WK sounding, facilitating comparison with the numerical and theoretical solutions. However, since R was not analyzed in their study, a characteristic updraft radius $R \sim 7\Delta x$ is assumed here consistent with the effective resolution reported for similar squall-line simulations[2] (Skamarock 2004). It is possible that the maximum w could be associated with updrafts smaller than the effective resolution, although this seems unlikely given the expectation of substantially increased entrainment in such updrafts from computational (numerical) mixing. Another challenge for this comparison is that the theoretical and numerical solutions assume an unsheared environment, while the simulations had an environment with fairly strong low-level vertical shear (17.5 m s^{-1} difference in u over the lowest 2.5 km). Nonetheless, as argued in Part I, the role of buoyant perturbation pressure is still important for sheared environments, so that the

[2] W97 used fourth-order centered advection plus fourth-order horizontal smoothing. They also included "physical mixing" using an eddy diffusion coefficient calculated from a prognostic turbulence kinetic energy scheme. Skamarock (2004) reported an effective resolution of $7\Delta x$ for simulations using implicit filtering from fifth-order upwind advection but found that simulations using second-order centered advection with small fourth-order smoothing (hyperviscosity coefficient of 4.25×10^8 m^4 s^{-1}) produced similar results to the fifth-order upwind advection in terms of kinetic energy spectra. While fourth-order centered advection plus fourth-order horizontal smoothing was not tested; an effective resolution of $7\Delta x$ for the W97 simulations is also assumed here.

TABLE 3. As in Table 2, but for a comparison of 2D fully dynamical updraft simulations and theoretical solutions. Results are illustrated at 550, 600, and 1020 s for the 1.5-, 3-, and 10-km initial bubble radii simulations, respectively, when the updraft top reaches ~4.5 km in height.

					Δp (hPa)		Max w (m s^{-1})	
Initial warm-bubble radius (km)	R (km)	H (km)	CAPE (J kg^{-1})	α	SIM	TH	SIM	TH
1.5	2.2	2.4	224	0.47	112	118	16.4	13.3
3	3.3	2.6	250	0.48	153	162	11.7	11.2
10	5.4	2.6	260	0.57	184	205	9.0	6.6

theoretical and numerical scalings of w with R are expected to apply approximately in these conditions.

For a given R and dimensionality, the maximum w from W97 is consistently ~40% smaller than the theoretical and numerical calculations (Fig. 14a). This is expected because condensate loading and entrainment were neglected in the calculation of B for the numerical and theoretical w. There is also some uncertainty because horizontal distributions of B across updrafts are not known from the simulations (the COS distribution was used for the numerical and theoretical calculations in Figs. 14 and 15). Note that in general entrainment

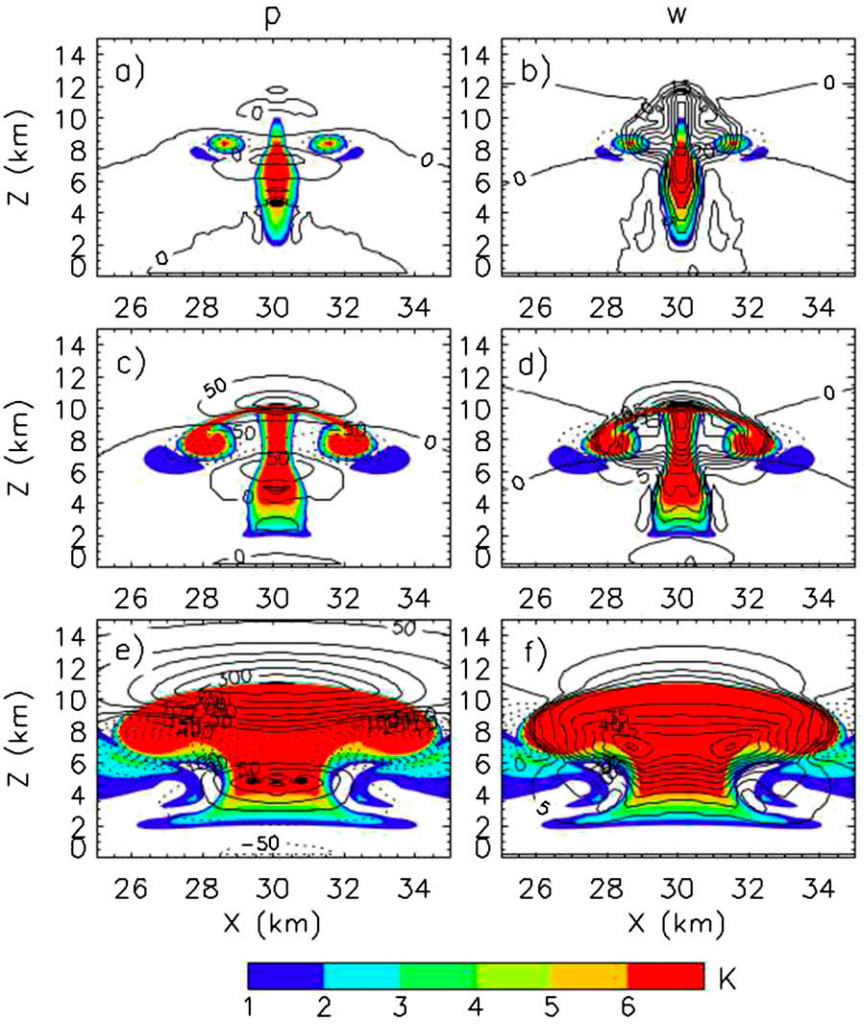

FIG. 13. As in Fig. 12, but for results later in the simulations when entrainment begins to dominate. The contour interval is 50 hPa for p and 5 m s^{-1} for w. Results are shown for times when the cloud top reaches ~9–10 km in height: 800, 800, and 1130 s for the initial bubble radii of 1.5, 3, and 10 km, respectively.

TABLE 4. As in Table 2, but for analysis at later times in the 3D simulations after entrainment begins to dominate. Results are illustrated at 800 (1130) s for the 1.5- and 3-km (10 km) initial bubble radii simulations, when the updraft top reaches 9–10 km in height.

Initial warm-bubble radius (km)	R (km)	H (km)	CAPE (J kg^{-1})	α	Δp (hPa)		Max w (m s^{-1})	
					SIM	TH	SIM	TH
1.5	1.8	7.4	905	0.38	9	10	42.6	42.2
3	2.8	8.8	1250	0.48	170	37	56.9	48.9
10	4.6	8.8	1730	0.75	387	252	47.0	51.4

may also be expected to depend on R, but at these relatively coarse grid spacings ($\Delta x \geq 1$ km) it seems unlikely there would be a strong dependence of entrainment on Δx for R larger than the approximate $7\Delta x$ computational filter scale (i.e., the effective resolution), given that W97 reported that computational mixing ''contributes much more to the net smoothing'' than physical (parameterized) mixing. Furthermore, if entrainment scales with R as $1/R$, as has been suggested by some studies (e.g., Simpson 1971), the fact that the simulated maximum w decrease with Δx suggests that entrainment plays a limited role in this sensitivity compared to perturbation pressure effects at these scales. That said, entrainment is likely to be more important for driving sensitivity to Δx for Δx of O (1) km and less, as suggested by Bryan and Morrison (2012) and Morrison et al. (2015a).

Despite these caveats, the scaling of w with R (Δx) is remarkably similar between the numerical and theoretical solutions and the fully dynamical simulations from W97 for both 2D and 3D; this is more clearly seen by uniformly scaling the analytic and numerical w by a factor of 0.6 (Fig. 14b). The W97 simulations also show weaker updrafts in 2D than 3D consistent with the numerical and theoretical calculations. Thus, the theoretical expressions appear to provide a concise explanation for relatively weak updrafts in 2D; this occurs as a direct result of differences in mass continuity between 2D and 3D as shown in Part I.

Comparing the hydrostatic simulations from W97 and the 2D and 3D theoretical expressions for hydrostatic w_N given by (34) and (35) in Part I provides insight into the scales at which nonhydrostatic effects become important (Fig. 15). A comparison of Figs. 15 and 14a shows that for this sounding, the theoretical nonhydrostatic and hydrostatic scalings diverge for R less than ~25–30 km for 3D and ~12–15 km for 2D, in qualitative agreement with the 2D and 3D simulations from W97, again with the assumption that $R \sim 7\Delta x$. Notably, the theoretical scalings are consistent with the hydrostatic–nonhydrostatic transition occurring at smaller R for 2D than 3D in the simulations (i.e., differences between the hydrostatic and nonhydrostatic maximum w from W97 are much larger for 2D than 3D for R of 14 and 28 km). The theoretical hydrostatic expressions give results closer in magnitude to W97 than the nonhydrostatic results. Reasons for this difference between the hydrostatic and nonhydrostatic results are unclear.

For many applications the total or horizontally averaged vertical fluxes of mass, momentum, static energy, water, and chemical constituents are key quantities with regard to moist convective dynamics. Studies have shown a wide range of behavior of the total vertical fluxes (mass or momentum) with an increase in Δx, from an increase (W97), to no consistent change (Morrison et al. 2015a), to a decrease (Moeng et al. 2010; Arakawa and Wu 2013; Bryan and Morrison 2012). As a result, it has proven challenging to understand this sensitivity from a broader conceptual standpoint.

The theoretical expressions relating w and R may provide some insight into this issue, if perturbation pressure plays a key role in driving sensitivity of convective strength to Δx in the gray zone as argued above. Since the area of an updraft A is approximately proportional to R^2 in 3D, and the total vertical mass flux is

TABLE 5. As in Table 4, but for a comparison of 2D fully dynamical updraft simulations and theoretical solutions. Results are illustrated at 1020, 1000, and 1400 s for the 1.5-, 3-, and 10-km initial bubble radii simulations, respectively, when the updraft top reaches 9–10 km in height.

Initial warm-bubble radius (km)	R (km)	H (km)	CAPE (J kg^{-1})	α	Δp (hPa)		Max w (m s^{-1})	
					SIM	TH	SIM	TH
1.5	3.2	5.4	258	0.54	160	72	23.7	16.8
3	3.0	7.0	504	0.58	296	120	21.7	26.0
10	3.6	6.4	1076	0.66	487	394	38.7	32.5

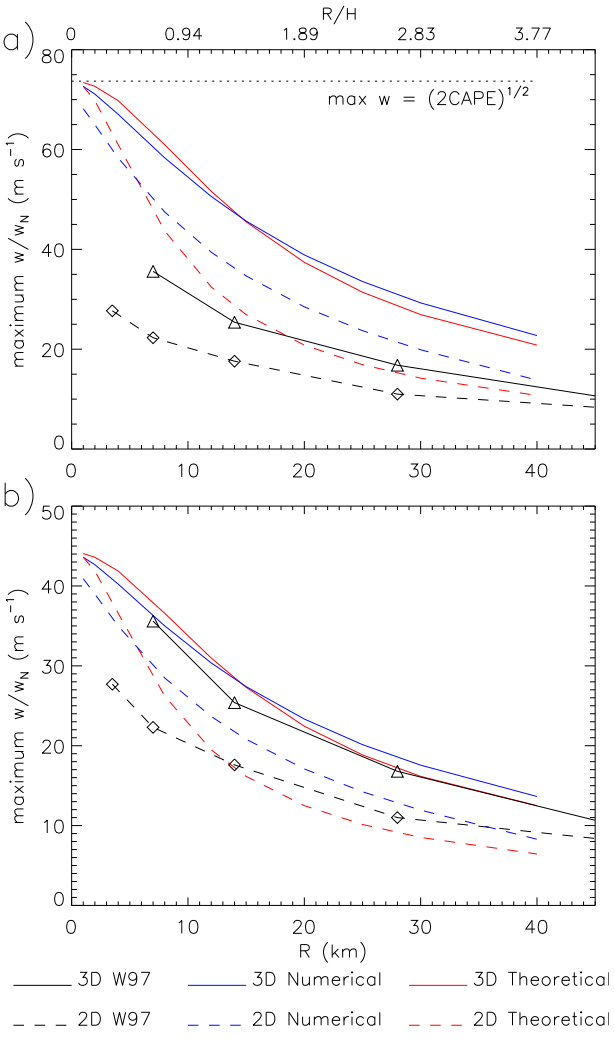

FIG. 14. (a) Comparison of w_N from the theoretical (red) and numerical (blue) solutions and maximum vertical velocity reported from simulations of W97 (black) as a function of R. (b) As in (a), except uniformly scaling the theoretical and numerical w_N by a factor of 0.6. Solid and dashed lines indicate calculations for 3D and 2D, respectively. For the simulations, it is assumed that the characteristic updraft radius scales as $7\Delta x$. The thermodynamic maximum w given by $\sqrt{2\text{CAPE}}$ is shown by the horizontal dotted line.

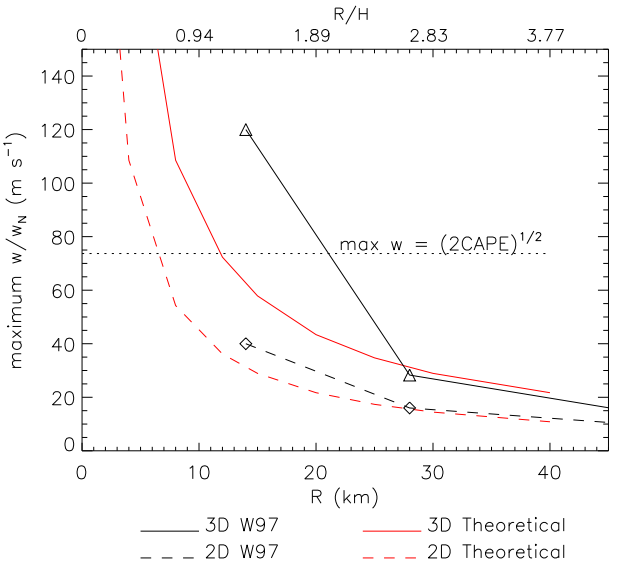

FIG. 15. Comparison of w_N from the hydrostatic theoretical expression (red) and maximum vertical velocity reported from the hydrostatic simulations of W97 (black) as a function of R. Solid and dashed lines indicate calculations for 3D and 2D, respectively. For the simulations, it is assumed that the characteristic updraft radius scales as $7\Delta x$. The thermodynamic maximum w given by $\sqrt{2\text{CAPE}}$ is shown by the horizontal dotted line.

given by $NA\overline{w} \sim NA\alpha w_0$, where N is the number of updraft cores and w_0 is the vertical velocity at the updraft center (assumed to be the maximum value horizontally), for $R/H \ll 1$ the analytic solutions in Part I suggests a total vertical mass flux that scales as NR^2, while in the hydrostatic regime ($R/H \gg 1$) the total mass flux scales with NRH. (Note that since a spectrum of updrafts with various R occurs in simulations, here R is meant to be a characteristic value in terms of the peak w kinetic energy associated with convective motions.) For 2D, the total mass flux scales with NR for $R/H \ll 1$ and NH in the hydrostatic regime based on similar arguments. Thus, when the vertical mass flux is not constrained ["Type 2" convection in Emanuel (1994)] it is hypothesized that a decrease (increase) in the total vertical mass flux should occur if N decreases with Δx at a rate faster (slower) than $1/R^2$ for $R/H \ll 1$, or $1/(RH)$ for the hydrostatic regime, in 3D (for a given CAPE). Analogously, these arguments suggest a decrease (increase) in the total vertical mass flux should occur if N decreases with Δx at a rate faster (slower) than $1/R$ for $R/H \ll 1$, or $1/H$ in the hydrostatic regime, for 2D. On the other hand, if the vertical mass flux is constrained in some way, for example, when convection is in quasi equilibrium with its environment ["Type I" convection in Emanuel (1994)], then N should decrease (increase) with Δx at a rate faster (slower) than $1/R^2$ for $R/H \ll 1$ if the total vertical mass flux decreases (increases), with analogous expressions for 2D and/or hydrostatic regimes. It is emphasized that entrainment may also play an important role in explaining sensitivities of the total vertical mass flux to Δx, especially for Δx of $O(1)$ km and less, which may be expected to alter these scalings.

b. *Implications for convection parameterizations*

In addition to mass flux closure and trigger formulations, convection parameterizations often include simplified entraining/detraining plume models to relate

updraft velocity to buoyancy and entrainment [for a review, see Siebesma et al. (2003)]:

$$\frac{1}{2}\frac{\partial(w^2)}{\partial z} = aB - b\varepsilon w^2, \tag{4}$$

where $\varepsilon = \lambda/L_e$ is an entrainment parameter (L_e is an entrainment length scale, generally assumed to be equal to R or z), a is a virtual mass coefficient, and b is an entrainment coefficient. The virtual mass coefficient, encapsulating perturbation pressure effects by scaling the buoyancy, is generally set to a constant and often without strong physical justification for particular values used (see the introduction). The theoretical expressions in Part I give a pressure scaling of w of the same form as the virtual mass coefficient in (4) and, hence, provide a concise physical interpretation of "a" by relating it to α, R, H, and H_1 via (20) and (27) in Part I.

The proposed theoretical expressions also provide a consistent way to include perturbation pressure effects in convection parameterizations. This can be done analytically by squaring the expressions in (2) and (3), taking $\partial/\partial z$, rearranging terms, and combining with (4) to yield

$$\frac{1}{2}\frac{\partial(w^2)}{\partial z} = \left(1 + \frac{\alpha^2 R^2}{H_1^2}\right)^{-1} B - b\varepsilon w^2 \quad z \le z_M \quad \text{and} \tag{5}$$

$$\frac{1}{2}\frac{\partial(w^2)}{\partial z} = \left[1 + \gamma_1 + \frac{(z - z_M)}{H_2}(\gamma_2 - \gamma_1)\right]^{-1} B - \left[1 + \gamma_1 + \frac{(z - z_M)}{H_2}(\gamma_2 - \gamma_1)\right]^{-2} \frac{(\gamma_2 - \gamma_1)}{H_2} \int_{z_F}^{z} B\, dz - b\varepsilon w^2 \quad z > z_M, \tag{6}$$

where z_F and z_M are the heights of the LFC and LMB, respectively, $\gamma_1 = \alpha^2 R^2/H_1^2$ and $\gamma_2 = 2\alpha^2 R^2/H^2$. Equations (5) and (6) can be combined with equations for the vertical derivative of total water mixing ratio and liquid water potential temperature [see (10) in Siebesma et al. (2003)] to include effects of entrainment on B; this provides a simple set of coupled ordinary differential equations for calculating vertical profiles of B and w. When certain functional forms are assumed for ε (e.g., $\varepsilon \sim 1/R$), approximate analytic solutions for $w(z)$ and $B(z)$ can also be derived. Further analysis and testing of (5) and (6) and discussion of analytic solutions is left for future work. Note that dynamic perturbation pressure can also influence vertical profiles of w in the updraft core, especially for relatively narrow updrafts, even though the overall impact on acceleration of w is limited (see Part I, section 2). Including these effects of p_D is also left for future work.

5. Summary and conclusions

This study investigated the role of perturbation pressure on the vertical velocity w of buoyant updraft cores in an unsheared environment. In the current paper, Part II, analytic theoretical solutions for the perturbation pressure difference from the LNB to LFC, Δp, and w as a function of updraft radius R, height H, and CAPE from Part I were compared to numerical solutions of the anelastic buoyant perturbation pressure Poisson equation. Several thermal buoyancy profiles derived from real and idealized thermodynamic soundings representing shallow to deep moist convection were tested. Despite idealizations made in deriving the theoretical expressions, the theoretical and numerical solutions showed a close correspondence for both 2D and 3D over a wide range of R. The theoretical and numerical solutions also gave similar differences in Δp and w between 2D and 3D updraft geometries. These differences were a direct consequence of fundamental differences in mass continuity between 2D and 3D as shown in Part I and were quantitatively consistent with differences between the 2D and 3D simulations from W97. This provides a physical explanation for weaker updrafts in 2D than 3D reported in many previous studies using fully dynamical models.

The theoretical expressions for Δp and maximum w were also similar to results from 2D and 3D fully dynamical simulations of moist convection initiated by warm bubbles of varying width. Differences between the theoretical and simulated Δp and maximum w were less than ~15% and ~25%, respectively, when the simulated updrafts were analyzed shortly after release of the bubbles to limit the role of entrainment. The theoretical Δp and w were also generally consistent with the simulations at later times once entrainment began to dominate, although differences were larger than earlier in the simulations. This was presumably because of entrainment, which led to a complicated structure of the buoyancy field in the simulations that was not taken into account in the theoretical derivation. Overall, these

results suggest the ability of the theoretical expressions to describe the behavior of updrafts when all dynamical processes are considered, including time-evolving terms neglected in the theoretical derivation.

Since R approximately scales with the effective model resolution (and hence is approximately proportional to Δx) in the "gray zone," with Δx of $O(1–10)$ km where convection is generally underresolved, these results suggest that an incorrect representation of perturbation pressure from spuriously wide updrafts may be important in explaining sensitivity of these models to Δx. This was illustrated by comparing the numerical and theoretical calculations of w_N with the maximum w from 2D and 3D fully dynamical simulations of W97. Despite caveats, the numerical and theoretical scalings of w with R were similar to the W97 simulations, assuming $R \sim 7\Delta x$—that is, assuming a characteristic R that scales with an estimate of the effective model resolution. The magnitudes of the theoretical and numerical w were ~40% larger, presumably because condensate loading and entrainment were neglected.

These results suggest that modifying the treatment of parameterized subgrid-scale mixing alone, such as changing the mixing lengths, may not address the root cause of biases in convective strength and vertical transport in gray-zone models if these biases are fundamentally related to updrafts that are too wide, leading to incorrect perturbation pressure effects. This also suggests challenges in applying improved mixing parameterizations (e.g., Moeng et al. 2010; Arakawa and Wu 2013; Wu and Arakawa 2014; Bogenschutz and Kruger 2013) to better partition the resolved and subgrid-scale (SGS) or subfilter-scale (SFS) fluxes as a function of Δx in these models. If the dominant scales of buoyant production of w kinetic energy in updraft cores are underresolved, leading to incorrect buoyant production of w kinetic energy because of updrafts that are too wide, then the total (or horizontally averaged) fluxes may be incorrect even if the "correct" partitioning of resolved and SGS/SFS fluxes is applied. Furthermore, the resolved vertical fluxes are not necessarily underpredicted in the gray zone despite underresolving convection. For example, W97 found an increase in the horizontally averaged vertical fluxes of momentum and potential temperature as Δx was increased from 1 to 12 km. If the SGS/SFS fluxes increase with increasing Δx, as we expect they should, then applying the "correct" partitioning of SGS/SFS and resolved fluxes in this instance would increase the bias of excessive fluxes, relative to the $\Delta x = 1$ km simulation from W97.

The theoretical expressions relating w and R herein may provide some insight into these issues. Based on these expressions, scalings were hypothesized that relate the total vertical mass flux to the number and size of convective updraft cores in 2D and 3D. These scalings suggest either an increase or decrease of the total vertical mass flux depending on how N (number of updraft cores) and the characteristic R change with Δx. Further work is needed to test these scalings and to determine how these sensitivities to R (Δx) are also affected by entrainment, which is expected to be especially important for Δx of $O(1)$ km and less. Difficulty in clearly defining and differentiating updraft cores is also noted (Sherwood et al. 2013) and poses challenges for such an effort. Nonetheless, these scalings potentially provide a useful context for improved understanding of the sensitivity of vertical mass fluxes to Δx in gray-zone models.

Plume models in convection parameterizations often rely on a simple treatment of perturbation pressure effects on w by reducing the buoyancy using a "virtual mass" coefficient that is constant or parameterized in an ad hoc way. The theoretical solutions from Part I provide a concise physical interpretation of the virtual mass coefficient in terms of α, R, and H and can, therefore, provide guidance for how this parameter might vary under a range of conditions. Based on the theoretical derivation, simple expressions were proposed that incorporate perturbation pressure effects in a more realistic way, including a dependence on R and H, for little computational cost. Additional testing and analysis of these expressions for updraft vertical velocity, including the effects of entrainment, is left for future work. The importance of the parameter α in the theoretical expressions (which relates w at the updraft center to its horizontal average across the updraft) is also noted. This was treated as an externally specified parameter in this study but it should be intrinsically linked to entrainment since it depends on how w varies horizontally across the updraft. Work is needed to better characterize typical values of α and how they relate to entrainment of momentum and B under various conditions.

Acknowledgments. This work was partially supported by U.S. DOE ASR DE-SC0008648, NASA NNX14AO85G, and the NSF Science and Technology Center for Multiscale Modeling of Atmospheric Processes (CMMAP), managed by Colorado State University under Cooperative Agreement ATM-0425247. The author thanks G. Bryan, R. Rotunno, W. Grabowski, and Z. Lebo for relevant discussions, R. Rotunno and W. Grabowski for comments on an earlier version of the manuscript, G. Bryan for developing and maintaining CM1, and P. Markowski for code used to separate the various contributions of perturbation pressure in CM1. NCAR's Computer Information Systems Laboratory is

acknowledged for providing the Poisson solver as part of the MUDPACK library.

REFERENCES

Adlerman, E. J., and K. K. Droegemeier, 2002: The sensitivity of numerically simulated cyclic mesocyclogenesis to variations in model physical and computational parameters. *Mon. Wea. Rev.*, **130**, 2671–2691, doi:10.1175/1520-0493(2002)130<2671:TSONSC>2.0.CO;2.

Arakawa, A., and C.-M. Wu, 2013: A unified representation of deep moist convection in numerical modeling of the atmosphere. Part I. *J. Atmos. Sci.*, **70**, 1977–1992, doi:10.1175/JAS-D-12-0330.1.

Bechtold, P., E. Bazile, F. Guichard, P. Mascart, and E. Richard, 2001: A mass-flux convection scheme for regional and global models. *Quart. J. Roy. Meteor. Soc.*, **127**, 869–886, doi:10.1002/qj.49712757309.

Bélair, S., and J. Mailhot, 2001: Impact of horizontal resolution on the numerical simulation of a midlatitude squall line: Implicit versus explicit condensation. *Mon. Wea. Rev.*, **129**, 2362–2376, doi:10.1175/1520-0493(2001)129<2362:IOHROT>2.0.CO;2.

Bogenschutz, P. A., and S. K. Kruger, 2013: A simplified PDF parameterization of subgrid-scale clouds and turbulence for cloud-resolving models. *J. Adv. Model. Earth Syst.*, **5**, 195–211, doi:10.1002/jame.20018.

Bretherton, C. S., J. R. McCaa, and H. Grenier, 2004: A new parameterization for shallow cumulus convection and its application to marine subtropical cloud-topped boundary layers. Part I: Description and 1D results. *Mon. Wea. Rev.*, **132**, 864–882, doi:10.1175/1520-0493(2004)132<0864:ANPFSC>2.0.CO;2.

Bryan, G. H., and J. M. Fritsch, 2002: A benchmark simulation for moist nonhydrostatic numerical models. *Mon. Wea. Rev.*, **130**, 2917–2928, doi:10.1175/1520-0493(2002)130<2917:ABSFMN>2.0.CO;2.

——, and H. Morrison, 2012: Sensitivity of a simulated squall line to horizontal resolution and parameterization of microphysics. *Mon. Wea. Rev.*, **140**, 202–225, doi:10.1175/MWR-D-11-00046.1.

——, J. C. Wyngaard, and J. M. Fritsch, 2003: Resolution requirements for the simulation of deep moist convection. *Mon. Wea. Rev.*, **131**, 2394–2416, doi:10.1175/1520-0493(2003)131<2394:RRFTSO>2.0.CO;2.

Clark, A. J., and Coauthors, 2012: An overview of the 2010 Hazardous Weather Testbed Experimental Forecast Program Spring Experiment. *Bull. Amer. Meteor. Soc.*, **93**, 55–74, doi:10.1175/BAMS-D-11-00040.1.

Dawson, D. T., II, E. R. Mansell, Y. Jung, L. J. Wicker, M. R. Kumjian, and M. Xue, 2014: Low-level ZDR signatures in supercell forward flanks: The role of size sorting and melting of hail. *J. Atmos. Sci.*, **71**, 276–299, doi:10.1175/JAS-D-13-0118.1.

de Roode, S. R., A. P. Siebesma, H. J. J. Jonker, and Y. de Voogd, 2012: Parameterization of the vertical velocity equation for shallow cumulus clouds. *Mon. Wea. Rev.*, **140**, 2424–2436, doi:10.1175/MWR-D-11-00277.1.

de Rooy, W. C., and A. P. Siebesma, 2010: Analytic expressions for entrainment and detrainment in cumulus convection. *Quart. J. Roy. Meteor. Soc.*, **136**, 1216–1227, doi:10.1002/qj.640.

Donner, L. J., 1993: A cumulus parameterization including mass fluxes, vertical momentum dynamics, and mesoscale effects. *J. Atmos. Sci.*, **50**, 889–906, doi:10.1175/1520-0469(1993)050<0889:ACPIMF>2.0.CO;2.

Emanuel, K. A., 1994: *Atmospheric Convection*. Oxford University Press, 580 pp.

Fiori, E., A. Parodi, and F. Siccardi, 2010: Turbulence closure parameterization and grid spacing effects in simulated supercell storms. *J. Atmos. Sci.*, **67**, 3870–3890, doi:10.1175/2010JAS3359.1.

Gentry, M. S., and G. M. Lackmann, 2010: Sensitivity of simulated tropical cyclone structure and intensity to horizontal resolution. *Mon. Wea. Rev.*, **138**, 688–704, doi:10.1175/2009MWR2976.1.

Grabowski, W. W., 2001: Coupling cloud processes with the large-scale dynamics using the Cloud-Resolving Convection Parameterization (CRCP). *J. Atmos. Sci.*, **58**, 978–997, doi:10.1175/1520-0469(2001)058<0978:CCPWTL>2.0.CO;2.

Gregory, D., 2001: Estimation of entrainment rate in simple models of convective clouds. *Quart. J. Roy. Meteor. Soc.*, **127**, 53–72, doi:10.1002/qj.49712757104.

Holton, J. R., 1973: A one-dimensional cumulus model including pressure perturbations. *Mon. Wea. Rev.*, **101**, 201–205, doi:10.1175/1520-0493(1973)101<0201:AOCMIP>2.3.CO;2.

Jakob, C., and A. P. Siebesma, 2003: A new subcloud model for mass-flux convection schemes: Influence on triggering, updraft properties, and model climate. *Mon. Wea. Rev.*, **131**, 2765–2778, doi:10.1175/1520-0493(2003)131<2765:ANSMFM>2.0.CO;2.

Kain, J. S., 2004: The Kain–Fritsch convective parameterization: An update. *J. Appl. Meteor.*, **43**, 170–181, doi:10.1175/1520-0450(2004)043<0170:TKCPAU>2.0.CO;2.

——, and J. M. Fritsch, 1990: A one-dimensional entraining/detraining plume model and its application in convective parameterization. *J. Atmos. Sci.*, **47**, 2784–2802, doi:10.1175/1520-0469(1990)047<2784:AODEPM>2.0.CO;2.

——, and Coauthors, 2008: Some practical considerations regarding horizontal resolution in the first generation of operational convection-allowing NWP. *Wea. Forecasting*, **23**, 931–952, doi:10.1175/WAF2007106.1.

Khairoutdinov, M. F., and D. A. Randall, 2001: A cloud resolving model as a cloud parameterization in the NCAR Community Climate System Model: Preliminary results. *Geophys. Res. Lett.*, **28**, 3617–3620, doi:10.1029/2001GL013552.

Kuang, Z., and C. S. Bretherton, 2006: A mass-flux view of a high-resolution simulation of shallow to deep cumulus convection. *J. Atmos. Sci.*, **63**, 1895–1909, doi:10.1175/JAS3723.1.

Lean, H. W., P. A. Clark, M. Dixon, N. M. Roberts, A. Fitch, R. Forbes, and C. Halliwell, 2008: Characteristics of high-resolution versions of the Met Office Unified Model for forecasting convection over the United Kingdom. *Mon. Wea. Rev.*, **136**, 3408–3424, doi:10.1175/2008MWR2332.1.

Lipps, F. B., and R. S. Hemler, 1986: Numerical simulation of deep tropical convection associated with large-scale convergence. *J. Atmos. Sci.*, **43**, 1796–1816, doi:10.1175/1520-0469(1986)043<1796:NSODTC>2.0.CO;2.

Markowski, P., and Y. Richardson, 2010: *Mesoscale Meteorology in Midlatitudes*. Wiley-Blackwell, 430 pp.

Miura, H., M. Satoh, T. Nasuno, A. T. Noda, and K. Oouchi, 2007: A Madden-Julian oscillation event realistically simulated by a global cloud-resolving model. *Science*, **318**, 1763–1765, doi:10.1126/science.1148443.

Moeng, C.-H., P. P. Sullivan, M. F. Khairoutdinov, and D. A. Randall, 2010: A mixed scheme for subgrid-scale fluxes in cloud-resolving models. *J. Atmos. Sci.*, **67**, 3692–3705, doi:10.1175/2010JAS3565.1.

Morrison, H., 2016: Impacts of updraft size and dimensionality on the perturbation pressure and vertical velocity in cumulus convection. Part I: Derivation of simple, generalized analytic solutions. *J. Atmos. Sci.*, **73**, 1441–1454, doi:10.1175/JAS-D-15-0040.1.

——, J. A. Milbrandt, G. H. Bryan, K. Ikeda, S. A. Tessendorf, and G. Thompson, 2015a: Parameterization of cloud microphysics based on the prediction of bulk ice particle properties. Part II: Case study comparisons with observations and other schemes. *J. Atmos. Sci.*, **72**, 312–339, doi:10.1175/JAS-D-14-0066.1.

——, A. Morales, and C. Villanueva-Birriel, 2015b: Concurrent sensitivities of an idealized deep convective storm to parameterization of microphysics, horizontal grid resolution, and environmental static stability. *Mon. Wea. Rev.*, **143**, 2082–2104, doi:10.1175/MWR-D-14-00271.1.

Neggers, R. A. J., M. Köhler, and A. C. M. Belijaars, 2009: A dual mass flux framework for boundary layer convection. Part I: Transport. *J. Atmos. Sci.*, **66**, 1464–1487, doi:10.1175/2008JAS2635.1.

Park, S., 2014: A unified convection scheme (UNICON). Part I: Formulation. *J. Atmos. Sci.*, **71**, 3902–3930, doi:10.1175/JAS-D-13-0233.1.

Parker, M. D., 2010: Relationship between system slope and updraft intensity in squall lines. *Mon. Wea. Rev.*, **138**, 3572–3578, doi:10.1175/2010MWR3441.1.

Pauluis, O., and S. Garner, 2006: Sensitivity of radiative–convective equilibrium simulations to horizontal resolution. *J. Atmos. Sci.*, **63**, 1910–1923, doi:10.1175/JAS3705.1.

Petch, J. C., and M. E. B. Gray, 2001: Sensitivity studies using a cloud-resolving model simulation of the tropical west Pacific. *Quart. J. Roy. Meteor. Soc.*, **127**, 2287–2306, doi:10.1002/qj.49712757705.

——, A. R. Brown, and M. E. B. Gray, 2002: The impact of horizontal resolution on the simulations of convective development over land. *Quart. J. Roy. Meteor. Soc.*, **128**, 2031–2044, doi:10.1256/003590002320603511.

Phillips, V. T. J., and L. J. Donner, 2006: Cloud microphysics, radiation and vertical velocities in two- and three-dimensional simulations of deep convection. *Quart. J. Roy. Meteor. Soc.*, **132**, 3011–3033, doi:10.1256/qj.05.171.

Redelsperger, J. L., and Coauthors, 2000: A GCSS model intercomparison for a tropical squall line observed during TOGA-COARE. I: Cloud-resolving models. *Quart. J. Roy. Meteor. Soc.*, **126**, 823–863, doi:10.1002/qj.49712656404.

Schlesinger, R. E., 1984: Effects of the pressure perturbation field in numerical models of unidirectionally sheared thunderstorm convection: Two versus three dimensions. *J. Atmos. Sci.*, **41**, 1571–1587, doi:10.1175/1520-0469(1984)041<1571:EOTPPF>2.0.CO;2.

Sherwood, S. C., D. Hernandaz-Deckers, M. Colin, and F. Robinson, 2013: Slippery thermals and cumulus entrainment paradox. *J. Atmos. Sci.*, **70**, 2426–2442, doi:10.1175/JAS-D-12-0220.1.

Siebesma, A. P., and Coauthors, 2003: A large eddy simulation intercomparison study of shallow cumulus convection. *J. Atmos. Sci.*, **60**, 1201–1219, doi:10.1175/1520-0469(2003)60<1201:ALESIS>2.0.CO;2.

Simpson, J., 1971: On cumulus entrainment and one-dimensional models. *J. Atmos. Sci.*, **28**, 449–455, doi:10.1175/1520-0469(1971)028<0449:OCEAOD>2.0.CO;2.

——, and V. Wiggert, 1969: Models of precipitating cumulus towers. *Mon. Wea. Rev.*, **97**, 471–489, doi:10.1175/1520-0493(1969)097<0471:MOPCT>2.3.CO;2.

Skamarock, W. C., 2004: Evaluating mesoscale NWP models using kinetic energy spectra. *Mon. Wea. Rev.*, **132**, 3019–3032, doi:10.1175/MWR2830.1.

Tao, W.-K., J. Simpson, and S.-T. Soong, 1987: Statistical properties of a cloud ensemble: A numerical study. *J. Atmos. Sci.*, **44**, 3175–3187, doi:10.1175/1520-0469(1987)044<3175:SPOACE>2.0.CO;2.

——, and Coauthors, 2009: A multiscale modeling system developments, applications, and critical issues. *Bull. Amer. Meteor. Soc.*, **90**, 515–534, doi:10.1175/2008BAMS2542.1.

vanZanten, M. C., and Coauthors, 2011: Controls on precipitation and cloudiness in simulations of trade-wind cumulus as observed during RICO. *J. Adv. Model. Earth Syst.*, **3**, M06001, doi:10.1029/2011MS000056.

Verelle, A., D. Ricard, and C. Lac, 2015: Sensitivity of high-resolution idealized simulations of thunderstorms to horizontal resolution and turbulence parameterization. *Quart. J. Roy. Meteor. Soc.*, **141**, 433–448, doi:10.1002/qj.2363.

Wang, X., and M. Zhang, 2014: Vertical velocity in shallow convection for different plume types. *J. Adv. Model. Earth Syst.*, **6**, 478–489, doi:10.1002/2014MS000318.

Weisman, M. L., and J. B. Klemp, 1982: The dependence of numerically simulated convective storms on vertical wind shear and buoyancy. *Mon. Wea. Rev.*, **110**, 504–520, doi:10.1175/1520-0493(1982)110<0504:TDONSC>2.0.CO;2.

——, W. C. Skamarock, and J. B. Klemp, 1997: The resolution dependence of explicitly modeled convective systems. *Mon. Wea. Rev.*, **125**, 527–548, doi:10.1175/1520-0493(1997)125<0527:TRDOEM>2.0.CO;2.

——, C. A. Davis, W. Wang, and K. Manning, 2008: Experiences with 0–36-h explicit convective forecasts with the WRF-ARW model. *Wea. Forecasting*, **23**, 407–437, doi:10.1175/2007WAF2007005.1.

Wilhelmson, R., 1974: The life cycle of a thunderstorm in three dimensions. *J. Atmos. Sci.*, **31**, 1629–1651, doi:10.1175/1520-0469(1974)031<1629:TLCOAT>2.0.CO;2.

Wu, C.-M., and A. Arakawa, 2014: A unified representation of deep moist convection in numerical modeling of the atmosphere. Part II. *J. Atmos. Sci.*, **71**, 2089–2103, doi:10.1175/JAS-D-13-0382.1.

Zeng, X., W.-K. Tao, S. Lang, A. Y. Hou, M. Zhang, and J. Simpson, 2008: On the sensitivity of atmospheric ensembles to cloud microphysics in long-term cloud-resolving model simulations. *J. Meteor. Soc. Japan*, **86A**, 45–65, doi:10.2151/jmsj.86A.45.